



General-relativistic Radiation Transport Scheme in Gmnu. I. Implementation of Two-moment-based Multifrequency Radiative Transfer and Code Tests

Patrick Chi-Kit Cheong (張志杰)^{1,2,8} , Harry Ho-Yin Ng³ , Alan Tsz-Lok Lam⁴ , and Tjonnie Guang Feng Li^{5,6,7} 

¹Department of Physics & Astronomy, University of New Hampshire, 9 Library Way, Durham NH 03824, USA

²Department of Physics, University of California, Berkeley, Berkeley, CA 94720, USA; patrick.cheong@berkeley.edu

³Institut für Theoretische Physik, Goethe Universität, Max-von-Laue-Str. 1, D-60438 Frankfurt am Main, Germany

⁴Max Planck Institute for Gravitational Physics (Albert Einstein Institute), Am Mühlenberg 1, Postdam-Golm D-14476, Germany

⁵Department of Physics and Astronomy, KU Leuven, Celestijnenlaan 200D, B-3001 Leuven, Belgium

⁶Department of Electrical Engineering (ESAT), KU Leuven, Kasteelpark Arenberg 10, B-3001 Leuven, Belgium

⁷Department of Physics, The Chinese University of Hong Kong, Shatin, N.T., Hong Kong

Received 2023 March 6; revised 2023 May 23; accepted 2023 May 24; published 2023 August 3

Abstract

We present the implementation of a two-moment-based general-relativistic multigroup radiation transport module in the General-relativistic multigrid numerical (Gmnu) code. On top of solving the general-relativistic magnetohydrodynamics and the Einstein equations with conformally flat approximations, the code solves the evolution equations of the zeroth- and first-order moments of the radiations in the Eulerian-frame. An analytic closure relation is used to obtain the higher order moments and close the system. The finite-volume discretization has been adopted for the radiation moments. The advection in spatial space and frequency-space are handled explicitly. In addition, the radiation–matter interaction terms, which are very stiff in the optically thick region, are solved implicitly. The implicit–explicit Runge–Kutta schemes are adopted for time integration. We test the implementation with a number of numerical benchmarks from frequency-integrated to frequency-dependent cases. Furthermore, we also illustrate the astrophysical applications in hot neutron star and core-collapse supernovae modelings, and compare with other neutrino transport codes.

Unified Astronomy Thesaurus concepts: [Relativistic fluid dynamics \(1389\)](#); [Neutron stars \(1108\)](#); [Supernova neutrinos \(1666\)](#); [Hydrodynamical simulations \(767\)](#); [Astronomical simulations \(1857\)](#); [Magnetohydrodynamical simulations \(1966\)](#); [Radiative transfer simulations \(1967\)](#)

1. Introduction

Radiation transport plays a crucial role in many high energy astrophysical events. For instance, radiation cooling and transport can significantly affect the structure and behavior of black hole accretion disks (see, e.g., Fragile et al. 2012; Sądowski et al. 2013; Fragile et al. 2014; McKinney et al. 2014; Takahashi et al. 2016; Fragile et al. 2018). On the other hand, neutrinos are responsible for the transport of energy and lepton number in dense and hot scenarios. For example, neutrinos largely determine the properties of the matter ejected by neutron star mergers. This matter is responsible for part of the observational electromagnetic signatures powered by nuclear reactions, as well as the contribution to astrophysical nucleosynthesis (see, e.g., Dessart et al. 2009; Metzger & Fernández 2014; Perego et al. 2014; Sekiguchi et al. 2015; Radice et al. 2015; Foucart et al. 2016a; Sekiguchi et al. 2016; Perego et al. 2017; Fujibayashi et al. 2017, 2018; Fernández et al. 2019; Nedora et al. 2019; Miller et al. 2019; Fujibayashi et al. 2020a, 2020b; Estee et al. 2021; Just et al. 2022). Not only in the context of neutron star mergers, neutrinos also significantly affect the dynamics of the core collapse of massive stars, and are responsible for powering the explosion as supernovae (see, e.g.,

Janka 2012; Burrows 2013; Foglizzo et al. 2015; Lentz et al. 2015; Melson et al. 2015; O’Connor & Couch 2018a; Burrows et al. 2020; Bollig et al. 2021; Burrows & Vartanyan 2021). In order to have a better understanding of such high energy astrophysical systems, not only do we need general-relativistic magnetohydrodynamics simulations, but a proper treatment for radiation transport is essential.

The full Boltzmann transport equation needs to be solved for the evolution of radiation fields. Although in principle this can be solved exactly by using the short characteristic method (Davis et al. 2012), the S_N schemes (Sumiyoshi & Yamada 2012; Nagakura et al. 2014, 2017; Chan & Müller 2020; White et al. 2023), the spherical harmonics schemes (McClarren & Hauck 2010; Radice et al. 2013), the lattice Boltzmann methods (Weih et al. 2020a), the method of characteristic moment closure (Ryan & Dolence 2020), and the Monte Carlo method (Abdikamalov et al. 2012; Miller et al. 2019; Foucart et al. 2021; Kawaguchi et al. 2023), solving the Boltzmann equation exactly is usually not practical due to the high computational cost. In practice, simplified versions of the Boltzmann transport equation are solved approximately.

One widely adopted approach is to solve only the first few moments of the radiation distribution function based on the truncated moment formalism (Thorne 1981; Shibata et al. 2011; Cardall et al. 2013). For example, the flux-limited diffusion approximation scheme solves only the zeroth moment (Levermore & Pomraning 1981; Pomraning 1981). In this scheme, only the information of radiation intensity is available, while the propagation directions are not. The direction of radiation flow can be retained in an averaged fashion by solving the first moment as

⁸ Network for Neutrinos, Nuclear Astrophysics, and Symmetries (N3AS) postdoctoral fellow.



well; this is known as the two-moment scheme (Levermore 1984; Dubroca & Feugeas 1999). This approach has been applied in the context of neutron star merger (Wanajo et al. 2014; Foucart et al. 2015; Foucart et al. 2016b; Foucart et al. 2016a; Sekiguchi et al. 2015; Radice et al. 2022; see also the review by Foucart 2023), core-collapse supernovae (O’Connor 2015; Just et al. 2015; Roberts et al. 2016; Kuroda et al. 2016; O’Connor & Couch 2018a; Skinner et al. 2019; Laiu et al. 2021; Santos-Pérez et al. 2023; see also the review Mezzacappa et al. 2020), black hole accretions (Zanotti et al. 2011; Fragile et al. 2012; Sądowski et al. 2013; Fragile et al. 2014; McKinney et al. 2014; Takahashi et al. 2016; Fragile et al. 2018), and other purposes (González et al. 2007; Commerçon et al. 2011; Skinner & Ostriker 2013; Takahashi & Ohsuga 2013; Rivera-Paleo & Guzmán 2019; Melon Fuksman & Mignone 2019; Weih et al. 2020b; Anninos & Fragile 2020; López-Miralles et al. 2023) as well. Despite the recent progress of radiation transport modeling, the implementation of general-relativistic multispecies multigroup radiation magnetohydrodynamics codes, which include fully coupled radiation–matter interactions, is still not very common (but see a notable example Kuroda et al. 2016), but is essential for astrophysics modeling.

In this work, we extend Gmnu (Cheong et al. 2020, 2021, 2022; H. H.-Y. Ng et al. 2024, in preparation) by implementing the two-moment-based multifrequency multispecies general-relativistic radiation transport module. In particular, we evolve the zeroth- and first-order moments, and adopt the maximum-entropy closure (Minerbo 1978) to close the system. The advection in spatial space is handled by the standard high-resolution shock-capturing method with a small modification on the Harten–Lax–van Leer (HLL) flux (Harten et al. 1983) in order to reduce the asymptotic diffusion limit in the high opacity region. The advection in frequency-space is evolved explicitly in a way that the energy-momentum is conserved (Müller et al. 2010; Kuroda et al. 2016). As such, our code is able to capture the Doppler and gravitational redshift effects. The radiation–matter interaction terms are solved implicitly since they are very stiff in the optically thick region. As in our previous work (Cheong et al. 2022), we adopt the implicit–explicit (IMEX) Runge–Kutta time integrators (see, e.g., Ascher et al. 1997; Pareschi & Russo 2005) to implicitly handle the stiff source terms while keeping the time step reasonable. These schemes have been applied and tested in several radiation hydrodynamics codes (e.g., Weih et al. 2020b; Anninos & Fragile 2020; Laiu et al. 2021; Izquierdo et al. 2023). We test the implementation with a number of numerical benchmarks, ranging from special-relativistic to general-relativistic, from optically thick to optically thin and from frequency-integrated to frequency-dependent cases. Moreover, we also include core-collapse supernova and hot neutron star modeling as astrophysical application examples. We then compare the result with other neutrino (magneto) hydrodynamics codes.

Accompanying this work, we have also developed a new neutrino microphysics library *Weakhub* (H. H.-Y. Ng et al. 2024, in preparation). This library includes the state-of-the-art neutrino microphysics, and provides advanced neutrino opacities and kernels that are essential to neutron star mergers and core-collapse supernovae modelings. Since the main focus of this work is to present and test the implementation of our new radiative transfer hydrodynamics module, the details of the neutrino microphysics are not included in this paper. For a

formal discussion of neutrino microphysics, we refer readers to H. H.-Y. Ng et al. (2024, in preparation).

The paper is organized as follows. In Section 2, we outline the formalism we used in this work. The details of the methodology and implementation of our radiation transport module are presented in Section 3. The code tests and results with idealized neutrino opacities are presented in Section 4. The comparison of different neutrino transport code with a conventional set of neutrino opacities in the context of core-collapse supernovae and hot neutron star is presented in Section 5. This paper ends with a discussion in Section 6.

Unless explicitly stated, the units of the speed of light c , gravitational constant G , solar mass M_\odot , and the Boltzmann constant k_B are all equal to 1 ($c = G = M_\odot = k_B = 1$). Greek indices, running from 0 to 3, are used for 4-quantities while the Roman indices, running from 1 to 3, are used for 3-quantities.

2. Formulations

The comoving-frame zeroth-, first-, second-, and third-order moments are defined as (Cardall et al. 2013; Mezzacappa et al. 2020)

$$\begin{aligned}\mathcal{J}(x^\mu, \nu) &\equiv \frac{\nu}{4\pi} \int f(x^\mu, \nu, \Omega) d\Omega, \\ \mathcal{H}^\alpha(x^\mu, \nu) &\equiv \frac{\nu}{4\pi} \int \ell^\alpha f(x^\mu, \nu, \Omega) d\Omega, \\ \mathcal{K}^{\alpha\beta}(x^\mu, \nu) &\equiv \frac{\nu}{4\pi} \int \ell^\alpha \ell^\beta f(x^\mu, \nu, \Omega) d\Omega, \\ \mathcal{L}^{\alpha\beta\gamma}(x^\mu, \nu) &\equiv \frac{\nu}{4\pi} \int \ell^\alpha \ell^\beta \ell^\gamma f(x^\mu, \nu, \Omega) d\Omega,\end{aligned}\quad (1)$$

where f is the distribution function, ℓ^α is the unit three-vector tangent to the three-momentum in the comoving frame, and namely, $u_\mu \ell^\mu = 0$. ν is the frequency of radiation observed in the comoving frame while $d\Omega$ is the solid angle in the comoving frame.

The monochromatic energy-momentum tensor $\mathcal{T}^{\mu\nu}$ and the corresponding third-rank momentum moment $\mathcal{U}^{\mu\nu\rho}$ can be Lagrangian decomposed with respect to the comoving observer with four-velocity u^μ as follows:

$$\mathcal{T}^{\mu\nu} = \mathcal{J}u^\mu u^\nu + \mathcal{H}^\mu u^\nu + u^\mu \mathcal{H}^\nu + \mathcal{K}^{\mu\nu}; \quad (2)$$

$$\begin{aligned}\mathcal{U}^{\mu\nu\rho} &= \nu(\mathcal{J}u^\mu u^\nu u^\rho + \mathcal{H}^\mu u^\nu u^\rho + u^\mu \mathcal{H}^\nu u^\rho + u^\mu u^\nu \mathcal{H}^\rho \\ &\quad + \mathcal{K}^{\mu\nu} u^\rho + \mathcal{K}^{\nu\rho} u^\mu + \mathcal{K}^{\rho\mu} u^\nu + \mathcal{L}^{\mu\nu\rho}),\end{aligned}\quad (3)$$

where $\mathcal{H}^\mu u_\mu$ and $\mathcal{K}^{\mu\nu} u_\mu = 0 = \mathcal{K}^{\mu\nu} u_\nu$. The corresponding frequency-integrated energy-momentum tensor of the radiation can be obtained by

$$T_{\text{rad}}^{\mu\nu} = \int_0^\infty 4\pi\nu^2 \mathcal{T}^{\mu\nu} d\nu = \int_0^\infty \mathcal{T}^{\mu\nu} dV_\nu; \quad (4)$$

where we have defined $dV_\nu \equiv 4\pi\nu^2 d\nu$.

Alternatively, the monochromatic energy-momentum tensor $\mathcal{T}^{\mu\nu}$ and the third-rank momentum moment $\mathcal{U}^{\mu\nu\rho}$ can be Eulerian decomposed with respect to the Eulerian observer with four-velocity n^μ as follows:

$$\begin{aligned}\mathcal{T}^{\mu\nu} &= \mathcal{E}n^\mu n^\nu + \mathcal{F}^\mu n^\nu + n^\mu \mathcal{F}^\nu + \mathcal{P}^{\mu\nu}; \\ \mathcal{U}^{\mu\nu\rho} &= \nu(\mathcal{Z}n^\mu n^\nu n^\rho + \mathcal{Y}^\mu n^\nu n^\rho + n^\mu \mathcal{Y}^\nu n^\rho + n^\mu n^\nu \mathcal{Y}^\rho \\ &\quad + \mathcal{X}^{\mu\nu} n^\rho + \mathcal{X}^{\nu\rho} n^\mu + \mathcal{X}^{\rho\mu} n^\nu + \mathcal{W}^{\mu\nu\rho}),\end{aligned}\quad (5)$$

where $\mathcal{F}^\mu n_\mu$ and $\mathcal{P}^{\mu\nu} n_\mu = 0 = \mathcal{P}^{\mu\nu} n_\nu$.

The evolution equations of the radiation can be obtained by

$$\nabla_\nu \mathcal{T}^{\mu\nu} - \frac{1}{\nu^2} \frac{\partial}{\partial \nu} (\nu^2 \mathcal{U}^{\mu\nu\rho} \nabla_\rho u_\nu) = \mathcal{S}_{\text{rad}}^\mu, \quad (6)$$

where $\mathcal{S}_{\text{rad}}^\mu$ is the radiation four-force, which describes the interaction between the radiation and the fluid.

The choice of the radiation four-force \mathcal{S}_{rad} depends on the type of radiation considered. In general, the radiation four-force contains the coupling between different radiation species at different frequencies group. By default, the radiation four-force \mathcal{S}_{rad} contains the emission and absorption source term $\mathcal{S}_{\text{E/A}}^\mu$, and the elastic (isoenergetic) scattering source term $\mathcal{S}_{\text{ES}}^\mu$:

$$\mathcal{S}_{\text{rad}}^\mu = \mathcal{S}_{\text{E/A}}^\mu + \mathcal{S}_{\text{ES}}^\mu, \quad (7)$$

and neglecting the frequency–species coupling. Here, the emission and absorption source term $\mathcal{S}_{\text{E/A}}^\mu$ and the elastic (isoenergetic) scattering source term $\mathcal{S}_{\text{ES}}^\mu$ are defined as

$$\mathcal{S}_{\text{E/A}}^\mu = [\eta - \kappa_a \mathcal{J}] u^\mu - \kappa_a \mathcal{H}^\mu; \quad (8)$$

$$\mathcal{S}_{\text{ES}}^\mu = -\kappa_s \mathcal{H}^\mu, \quad (9)$$

where η , κ_a , and κ_s are the radiation emissivity, absorption, and scattering coefficients, respectively.

It is worth pointing out that Gmunu has been designed to handle more sophisticated radiation four-forces where the frequency–species coupling is allowed (see Section 3.6.3 below). Since those interactions are application oriented, the discussion is not included in this section. An example of such complicated radiation four-force in the context of core-collapse supernovae can be found at Section 5.1 below.

2.1. General-relativistic Radiation Hydrodynamics in the Reference-metric Formalism

As in our previous work (Cheong et al. 2021, 2022; H. H.-Y. Ng et al. 2024, in preparation), we adopt 3 + 1 reference-metric formalism (Montero et al. 2014; Mewes et al. 2020; Baumgarte & Shapiro 2020). In this formalism, the metric can be written as

$$\begin{aligned} ds^2 &= g_{\mu\nu} dx^\mu dx^\nu \\ &= -\alpha^2 dt^2 + \gamma_{ij} (dx^i + \beta^i dt)(dx^j + \beta^j dt), \end{aligned} \quad (10)$$

where α is the lapse function, β^i is the space-like shift vector, and γ_{ij} is the spatial metric. We adopt a conformal decomposition of the spatial metric γ_{ij} with the conformal factor ψ :

$$\gamma_{ij} = \psi^4 \bar{\gamma}_{ij}, \quad (11)$$

where $\bar{\gamma}_{ij}$ is the conformally related metric. This conformally related metric can be expressed as the sum of a background *time-independent* reference metric $\hat{\gamma}_{ij}$ and deviations h_{ij}^{dev} . In our current implementation, the reference metric $\hat{\gamma}_{ij}$ is the flat spacetime metric of the chosen coordinate system (i.e., either Cartesian, cylindrical, or spherical coordinates). Note that, in conformally flat approximations, the spacetime deviations are vanishing, and the reference metric is the conformally related metric (i.e., $\bar{\gamma}_{ij} = \hat{\gamma}_{ij}$).

The evolution equations of the first two moments of radiations for each species of radiation at each frequency-group

(Equation (6)) can be written as

$$\begin{aligned} \frac{\partial}{\partial t} [\sqrt{\gamma/\hat{\gamma}} \mathcal{E}] &+ \hat{\nabla}_i [\sqrt{\gamma/\hat{\gamma}} (\alpha \mathcal{F}^i - \mathcal{E} \beta^i)] \\ &- \alpha \sqrt{\gamma/\hat{\gamma}} \frac{1}{\nu^2} \frac{\partial}{\partial \nu} [-\nu^2 n_\mu \mathcal{U}^{\mu\nu\rho} \nabla_\rho u_\nu] \\ &= \sqrt{\gamma/\hat{\gamma}} [-\mathcal{F}^j \partial_j \alpha + \mathcal{P}^{ij} K_{ij}] \\ &- \alpha \sqrt{\gamma/\hat{\gamma}} \mathcal{S}_{\text{rad}}^\mu n_{\mu}; \end{aligned} \quad (12)$$

$$\begin{aligned} \frac{\partial}{\partial t} [\sqrt{\gamma/\hat{\gamma}} \mathcal{F}_i] &+ \hat{\nabla}_i [\sqrt{\gamma/\hat{\gamma}} (\alpha \mathcal{P}_j^i - \mathcal{F}_j \beta^i)] \\ &- \alpha \sqrt{\gamma/\hat{\gamma}} \frac{1}{\nu^2} \frac{\partial}{\partial \nu} [\nu^2 \gamma_{i\mu} \mathcal{U}^{\mu\nu\rho} \nabla_\rho u_\nu] \\ &= \sqrt{\gamma/\hat{\gamma}} \left[-\mathcal{E} \partial_i \alpha + \mathcal{F}_k \hat{\nabla}_i \beta^k + \frac{1}{2} \alpha \mathcal{P}^{jk} \hat{\nabla}_i \gamma_{jk} \right] \\ &+ \alpha \sqrt{\gamma/\hat{\gamma}} \mathcal{S}_{\text{rad}}^\mu \gamma_{i\mu}, \end{aligned} \quad (13)$$

where the $\hat{\nabla}_i$ here is for the covariant derivatives associated with the reference metric $\hat{\gamma}_{ij}$.

As in our previous work (Cheong et al. 2021, 2022; H. H.-Y. Ng et al. 2024, in preparation), the evolution equations can be expressed as follows:

$$\begin{aligned} \partial_t \mathbf{q} &+ \frac{1}{\sqrt{\hat{\gamma}}} \partial_j [\sqrt{\hat{\gamma}} \mathbf{f}^j] + \frac{1}{\nu^2} \partial_\nu [\nu^2 \mathbf{f}_\nu] \\ &= \mathbf{s}_{\text{grav}} + \mathbf{s}_{\text{geom}} + \mathbf{s}_{\text{rad}}, \end{aligned} \quad (14)$$

where we denote

$$\mathbf{q} = \begin{bmatrix} q_\mathcal{E} \\ q_{\mathcal{F}_j} \end{bmatrix}, \mathbf{f}^i = \begin{bmatrix} (f_\mathcal{E})^i \\ (f_{\mathcal{F}_j})^i \end{bmatrix}, \mathbf{f}_\nu = \begin{bmatrix} f_{\nu\mathcal{E}} \\ f_{\nu\mathcal{F}_j} \end{bmatrix}, \mathbf{s} = \begin{bmatrix} s_\mathcal{E} \\ s_{\mathcal{F}_j} \end{bmatrix}. \quad (15)$$

Note that the subscript of the source terms in Equation (15) is omitted for a more compact expression. Here, \mathbf{q} s are the conserved quantities:

$$q_\mathcal{E} = \psi^6 \sqrt{\bar{\gamma}/\hat{\gamma}} \mathcal{E}; \quad (16)$$

$$q_{\mathcal{F}_j} = \psi^6 \sqrt{\bar{\gamma}/\hat{\gamma}} \mathcal{F}_j. \quad (17)$$

The corresponding fluxes \mathbf{f}^i are given by the following:

$$(f_\mathcal{E})^i = \psi^6 \sqrt{\bar{\gamma}/\hat{\gamma}} [\alpha \mathcal{F}^i - \mathcal{E} \beta^i]; \quad (18)$$

$$(f_{\mathcal{F}_j})^i = \psi^6 \sqrt{\bar{\gamma}/\hat{\gamma}} [\alpha \mathcal{P}_j^i - \mathcal{F}_j \beta^i]. \quad (19)$$

The fluxes in the frequency-space are as follows:

$$\begin{aligned} f_{\nu\mathcal{E}} &= \alpha \psi^6 \sqrt{\bar{\gamma}/\hat{\gamma}} [n_\mu \mathcal{U}^{\mu\nu\rho} \nabla_\rho u_\nu] \\ &= \psi^6 \sqrt{\bar{\gamma}/\hat{\gamma}} \nu \{ W [(Z^\nu - \mathcal{Y}^i) \partial_i \alpha - \mathcal{Y}_k \nu^i \partial_i \beta^k \\ &\quad - \alpha \mathcal{X}^{ki} \left(\frac{1}{2} \nu^m \partial_m \gamma_{ki} - K_{ki} \right)] \} \\ &\quad + [[Z \partial_t W - \mathcal{Y}_k \partial_t (W \nu^k)] + [\alpha \mathcal{Y}^i - Z \beta^i] \partial_i W \\ &\quad - [\alpha \mathcal{X}_k^i - \mathcal{Y}_k \beta^i] \partial_i (W \nu^k)], \end{aligned} \quad (20)$$

$$\begin{aligned}
f_{\nu\mathcal{F}_j} &= \alpha\psi^6\sqrt{\hat{\gamma}/\hat{\gamma}}[-\gamma_{i\mu}\mathcal{U}^{\mu\nu\rho}\nabla_\rho\mathbf{u}_\nu] \\
&= \psi^6\sqrt{\hat{\gamma}/\hat{\gamma}}\nu\left\{W[(\mathcal{Y}_j\nu^i - \mathcal{X}^i_j)\partial_t\alpha - \mathcal{X}_{jk}\nu^i\partial_i\beta^k\right. \\
&\quad \left. - \alpha\mathcal{W}_j^{ki}\left(\frac{1}{2}\nu^m\partial_m\gamma_{ki} - K_{ki}\right)\right] \\
&\quad + [(\mathcal{Y}_j\partial_t W - \mathcal{X}_{jk}\partial_t(W\nu^k))] + [\alpha\mathcal{X}^i_j - \mathcal{Y}_j\beta^i]\partial_i W \\
&\quad - [\alpha\mathcal{W}_j^{ki} - \mathcal{X}_{jk}\beta^i]\partial_i(W\nu^k)\}, \tag{21}
\end{aligned}$$

where ν^i is the fluid 3-velocity, and $W \equiv 1/\sqrt{1 - \nu^i\nu_i}$ is the Lorentz factor. For the details of the derivation, we refer readers to Cardall et al. (2013), Mezzacappa et al. (2020).

The corresponding gravitational source terms for s_{grav} are given by the following:

$$s_{\text{grav}\mathcal{E}} = \psi^6\sqrt{\hat{\gamma}/\hat{\gamma}}\{-\mathcal{F}^j\hat{\nabla}_j\alpha + \mathcal{P}^{ij}K_{ij}\}; \tag{22}$$

$$s_{\text{grav}\mathcal{F}_i} = \psi^6\sqrt{\hat{\gamma}/\hat{\gamma}}\left\{-\mathcal{E}\hat{\nabla}_i\alpha + \mathcal{F}_k\hat{\nabla}_i\beta^k + \frac{1}{2}\alpha\mathcal{P}^{jk}\hat{\nabla}_i\gamma_{jk}\right\}, \tag{23}$$

where K_{ij} is the extrinsic curvature. The only nonvanishing geometrical source terms for s_{geom} arising for the evolution equation of \mathcal{F}_i are

$$s_{\text{geom}\mathcal{E}} = 0; \tag{24}$$

$$s_{\text{geom}\mathcal{F}_i} = \hat{\Gamma}_{ik}^l(f_{\mathcal{F}_i})^k, \tag{25}$$

where the 3-Christoffel symbols $\hat{\Gamma}_{ik}^l$ associated with the reference metric $\hat{\gamma}_{ij}$. Finally, the radiation–matter coupling source terms for s_{rad} are given by

$$s_{\text{rad}\mathcal{E}} = -\alpha\sqrt{\gamma/\hat{\gamma}}\mathcal{S}_{\text{rad}}^\mu n_\mu; \tag{26}$$

$$s_{\text{rad}\mathcal{F}_i} = \alpha\sqrt{\gamma/\hat{\gamma}}\mathcal{S}_{\text{rad}}^\mu \gamma_{i\mu}. \tag{27}$$

2.2. Coupling to the Hydrodynamical and Metric Equations

The radiation fields contribute to the total energy-momentum tensor, which affects the hydrodynamical and metric equations. The hydrodynamical evolution equations are essentially the same as those in Cheong et al. (2021, 2022), except that the radiation four-force also arises in the source terms of energy and momentum equations, namely as follows:

$$s_\tau \rightarrow s_\tau - \sum_{\text{species}} \int s_{\text{rad}\mathcal{E}} dV_\nu; \tag{28}$$

$$s_{S_i} \rightarrow s_{S_i} - \sum_{\text{species}} \int s_{\text{rad}\mathcal{F}_i} dV_\nu. \tag{29}$$

To consistently solve the metric equations, the contribution of the radiations must be taken into account as well. This can be done simply by including the 3 + 1 decomposed source terms for radiation into our metric solver (Cheong et al. 2020, 2021). The 3 + 1 decomposed source terms for radiation can be obtained by

$$U_{\text{rad}} = \sum_{\text{species}} \{n_\mu n_\nu T_{\text{rad}}^{\mu\nu}\}, \tag{30}$$

$$S_{\text{rad}}^i = \sum_{\text{species}} \{-n_\mu \gamma_\nu^i T_{\text{rad}}^{\mu\nu}\}, \tag{31}$$

$$\text{and } S_{\text{rad}} = \sum_{\text{species}} \{\gamma_\mu^i \gamma_\nu^j T_{\text{rad}}^{\mu\nu}\}, \tag{32}$$

where $T_{\text{rad}}^{\mu\nu}$ is the frequency-integrated energy-momentum tensor (see Equation (4)) of the corresponding type of radiation.

3. Numerical Methods

3.1. Discretization

The discretization in the spatial and frequency-space for all quantities is based on the finite-volume approach.

An orthogonal system of coordinates (x^1, x^2, x^3) is discretized as follows. The computational domain is divided into $N_1 \times N_2 \times N_3$ cells, where each cell can be represented with a vector of integer numbers (i, j, k) and $1 \leq i \leq N_1$, $1 \leq j \leq N_2$ and $1 \leq k \leq N_3$. The cell bounds are given by $(x_{i-1/2}^1, x_{i+1/2}^1)$, $(x_{j-1/2}^2, x_{j+1/2}^2)$, and $(x_{k-1/2}^3, x_{k+1/2}^3)$, respectively. In other words, the mesh spacings can be represented as

$$\begin{aligned}
\Delta x_i^1 &= x_{i+1/2}^1 - x_{i-1/2}^1; \\
\Delta x_j^2 &= x_{j+1/2}^2 - x_{j-1/2}^2; \\
\Delta x_k^3 &= x_{k+1/2}^3 - x_{k-1/2}^3; \tag{33}
\end{aligned}$$

with the cell center

$$\begin{aligned}
x_i^1 &= \frac{1}{2}(x_{i+1/2}^1 + x_{i-1/2}^1); \\
x_j^2 &= \frac{1}{2}(x_{j+1/2}^2 + x_{j-1/2}^2); \\
x_k^3 &= \frac{1}{2}(x_{k+1/2}^3 + x_{k-1/2}^3). \tag{34}
\end{aligned}$$

The cell volume and the surface area, which are associated with the reference metric $\hat{\gamma}_{ij}$, are defined as

$$\Delta V \equiv \int_{\text{cell}} \sqrt{\hat{\gamma}} dx^1 dx^2 dx^3; \tag{35}$$

$$\Delta A^i \equiv \int_{\text{surface}} \sqrt{\hat{\gamma}} dx^{j \neq i}. \tag{36}$$

For the calculation of the cell volume ΔV , surface ΔA , and the 3-Christoffel symbols $\hat{\Gamma}_{ik}^l$, we refer readers to the appendix section in Cheong et al. (2021).

Additionally, the frequency-space is discretized by N_ν frequency-bins, where each bin can be represented with an integer $1 \leq f \leq N_\nu$, and the corresponding bounds are given by $(\nu_{f-1/2}, \nu_{f+1/2})$. The mesh spacing in the frequency-space can be written as

$$\Delta\nu_f = \nu_{f+1/2} - \nu_{f-1/2}, \tag{37}$$

and with the cell center

$$\nu_f = \frac{1}{2}(\nu_{f+1/2} + \nu_{f-1/2}). \tag{38}$$

In most of the cases, the frequency-bins are logarithmically spaced. Given the upper and lower bounds of the frequency-bins, $\nu_{\text{max}} \equiv \nu_{N_\nu+1/2}$, and $\nu_{\text{min}} \equiv \nu_{1/2}$, and the number of frequency-bins N_ν , the frequency-space can be discretized as the following. The $\Delta\nu$ for the first frequency-bin (at $f=1$) can be obtained by

$$\Delta\nu_1 = (\nu_{\text{max}} - \nu_{\text{min}}) \left(\frac{1 - q}{1 - q^{N_\nu}} \right), \tag{39}$$

where

$$q \equiv \left(\frac{\nu_{\max}}{\nu_{\min}} \right)^{1/N_\nu} \quad (40)$$

is the scale factor. The rest of the $\Delta\nu$ can be obtained by the recursion relation

$$\Delta\nu_{\bar{f}} = q\Delta\nu_{\bar{f}-1}. \quad (41)$$

With the relation between the width of the frequency-bin $\Delta\nu$ and also the corresponding cell interface and center (see Equations (37) and (38)), the grid of the frequency-space can be generated. The cell volume and the surface area in the 1D (spherically symmetric) frequency-space are as follows:

$$\Delta V_\nu \equiv \int_{\text{cell}} 4\pi\nu^2 d\nu; \quad \Delta A_\nu \equiv 4\pi\nu^2. \quad (42)$$

In Gmunu, the radiation quantities are volume-averaged in the spatial space and *frequency-integrated* in the momentum space. In particular, the quantity $\langle \mathbf{q} \rangle$ at the centroid (i, j, k, \bar{f}) and the cell interface ($i + 1/2, j, k, \bar{f}$) can be expressed as

$$\langle \mathbf{q} \rangle_{i,j,k,\bar{f}} \equiv \frac{1}{\Delta V_{i,j,k}} \int_{\Delta V_{i,j,k}} dV \int_{\Delta V_{\nu\bar{f}}} dV_\nu \mathbf{q}, \quad (43)$$

and

$$\langle \mathbf{q} \rangle_{i+1/2,j,k,\bar{f}} \equiv \frac{1}{\Delta A_{i+1/2,j,k}} \int_{\Delta A_{i+1/2,j,k}} dA \int_{\Delta V_{\nu\bar{f}}} dV_\nu \mathbf{q}, \quad (44)$$

respectively.

3.2. Higher Moments

Since only the first two moments (the zeroth- and first-moment \mathcal{E} and \mathcal{F}_i) are evolved (see Equations (12) and (13)) while the higher moments such as $\mathcal{P}^{\mu\nu}$ and $\mathcal{U}^{\mu\nu\rho}$ in general cannot be expressed in terms of \mathcal{E} and \mathcal{F}_i , a closure relation for determining the higher moments is needed to close the whole system.

In this work, we adopt the (approximate) analytic closure, which combines the optically thin and optically thick limits

$$\mathcal{P}^{\mu\nu} = d_{\text{thin}} \mathcal{P}_{\text{thin}}^{\mu\nu} + d_{\text{thick}} \mathcal{P}_{\text{thick}}^{\mu\nu}, \quad (45)$$

where $\mathcal{P}_{\text{thin}}^{\mu\nu}$ and $\mathcal{P}_{\text{thick}}^{\mu\nu}$ are the Eulerian-frame radiation pressure tensors in the optically thin and thick limit respectively. Here, we have defined

$$d_{\text{thin}} \equiv \frac{1}{2}(3\chi - 1); \quad d_{\text{thick}} \equiv \frac{3}{2}(1 - \chi), \quad (46)$$

where $\chi \in \left[\frac{1}{3}, 1 \right]$ is the Eddington factor. Similarly, the third moment in the fluid-frame, which is needed to compute the energy advection term, can be expressed as

$$\mathcal{L}^{\mu\nu\rho} = d_{\text{thin}} \mathcal{L}_{\text{thin}}^{\mu\nu\rho} + d_{\text{thick}} \mathcal{L}_{\text{thick}}^{\mu\nu\rho}. \quad (47)$$

In the optically thin limit, the radiation pressure tensor $\mathcal{P}_{\mu\nu}$ in the Eulerian-frame is chosen to be (see Shibata et al. 2011)

$$\mathcal{P}_{\text{thin}}^{\mu\nu} = \mathcal{E} \frac{\mathcal{F}^\mu \mathcal{F}^\nu}{\mathcal{F}^i \mathcal{F}_i}; \quad (48)$$

while the corresponding fluid-frame third moment is

$$\mathcal{L}_{\text{thin}}^{\mu\nu\rho} = \mathcal{J} \frac{\mathcal{H}^\mu \mathcal{H}^\nu \mathcal{H}^\rho}{(\mathcal{H}^2)^{3/2}}. \quad (49)$$

On the other hand, in the optically thick limit, where the fluid and radiation are in equilibrium, the radiation field is isotropic in the comoving frame

$$\mathcal{K}_{\text{thick}}^{\mu\nu} = \frac{1}{3} \mathcal{H}^{\mu\nu}; \quad (50)$$

where $h_{\mu\nu} = g_{\mu\nu} + u_\mu u_\nu$. Correspondingly, the radiation pressure tensor $\mathcal{P}_{\mu\nu}$ in the Eulerian-frame is

$$\mathcal{P}_{\text{thick}}^{\mu\nu} = \frac{4}{3} \mathcal{J} (W\nu^\mu)(W\nu^\nu) + \frac{1}{3} \mathcal{J} \gamma^{\mu\nu} + (\gamma_\alpha^\mu \mathcal{H}^\alpha)(W\nu^\nu) + (\gamma_\beta^\nu \mathcal{H}^\beta)(W\nu^\mu); \quad (51)$$

which can be expressed in the terms of the variables in the Eulerian-frame by

$$\frac{\mathcal{J}}{3} = \frac{1}{2W^2 + 1} [\mathcal{E}(2W^2 - 1) - 2W^2 \mathcal{F}^i v_i]; \quad (52)$$

$$\begin{aligned} \gamma_\beta^\alpha \mathcal{H}^\beta &= \frac{\mathcal{F}^\alpha}{W} + \frac{W\nu^\alpha}{2W^2 + 1} [(4W^2 + 1) \mathcal{F}^i v_i - 4W^2 \mathcal{E}] \\ &= \frac{\mathcal{F}^\alpha}{W} + W\nu^\alpha \left[\mathcal{F}^i v_i - \mathcal{E} - \frac{\mathcal{J}}{3} \right]. \end{aligned} \quad (53)$$

The fluid-frame third moment in the optically thick limit is

$$\mathcal{L}_{\text{thick}}^{\mu\nu\rho} = \frac{1}{5} (\mathcal{H}^\mu h^{\nu\rho} + \mathcal{H}^\nu h^{\rho\mu} + \mathcal{H}^\rho h^{\mu\nu}). \quad (54)$$

Note that Equation (48) is derived by assuming the radiation is symmetric around the direction parallel to the flux (Murchikova et al. 2017). Although this assumption is valid in spherical symmetry, this is not guaranteed in general cases. For instance, while this relation is asymptotically correct in the optically thick region, this is in general not the case in the free-streaming region because the radiation in the vacuum is not all propagating in the same direction (Foucart 2023). As a result, this approach fails to describe crossing radiation beams (see, e.g., Sądowski et al. 2013; Foucart et al. 2015; Weih et al. 2020b; Foucart 2023).

3.3. Closure Relation

A closure relation is needed to compute the Eddington factor χ . The choice of closure relation affects the accuracy of the two-moment solution. For more formal discussion and comparison of different analytic closure relations, we refer readers to Murchikova et al. (2017), Foucart (2018), and Richers (2020). In this work, we adopt the maximum-entropy closure (Minerbo 1978), which is given by

$$\chi(\zeta) = \frac{1}{3} + \zeta^2 \frac{2}{15} (3 - \zeta + 3\zeta^2); \quad (55)$$

where the flux factor ζ is defined as

$$\zeta \equiv \sqrt{\mathcal{H}^\mu \mathcal{H}_\mu / \mathcal{J}^2}. \quad (56)$$

In the optically thin limit, $\zeta \approx 1$, and thus $\chi \approx 1$. Conversely, in the optically thick limit, $\zeta \approx 0$, and thus $\chi \approx 1/3$.

Since the flux factor ζ is defined by the fluid-frame moments \mathcal{J} and \mathcal{H}_μ instead of the observer-frame moments \mathcal{E} and \mathcal{F}_μ , the

computation of ζ requires a root-finding process. As in Foucart et al. (2015), Weih et al. (2020b), we numerically find the root of

$$f(\zeta) = \frac{\zeta^2 \mathcal{J}^2 - \mathcal{H}^\mu \mathcal{H}_\mu}{\mathcal{E}^2}. \quad (57)$$

Since $f(\zeta)$ is smooth and its derivative can be expressed analytically, we numerically solve Equation (57) with the Newton–Raphson method, which is usually more efficient than bracketing methods. In case the Newton–Raphson method fails to converge, we use the Brent–Dekker method to solve this equation in the range $\zeta \in [0, 1]$.

3.4. Advection in Space

The numerical method for computing the fluxes for space advection is essentially the same as the high-resolution shock-capturing method, except that a slightly modified HLL Riemann solver from Harten et al. (1983) is used. As pointed out by multiple authors (e.g., O’Connor 2015; Foucart et al. 2015; Kuroda et al. 2016; Skinner et al. 2019; Weih et al. 2020b; Radice et al. 2022), the standard HLL Riemann solver would work only for the optically thin limit, while it fails to reduce the asymptotic diffusion limit when the opacity (absorption plus scattering) is large. To recover the asymptotic diffusion limit, in this work, we adopt the modification proposed in Audit et al. (2002), which has been applied in O’Connor & Ott (2013), Kuroda et al. (2016). To keep the notation compact, we discuss the approach in the x -direction for simplicity. Specifically, the HLL fluxes for \mathcal{E} and \mathcal{F}_i are modified as

$$f_{\mathcal{E}_{i+1/2}}^{\text{HLL}} = \frac{\lambda_+ F_- - \lambda_- F_+ + \delta_{i+1/2} \lambda_+ \lambda_- (q_+ - q_-)}{\lambda_+ - \lambda_-}; \quad (58)$$

$$f_{\mathcal{F}_{i+1/2}}^{\text{HLL}} = \frac{\delta_{i+1/2}^2 (\lambda_+ F_-^j - \lambda_- F_+^j) + \delta_{i+1/2} \lambda_+ \lambda_- (q_+^j - q_-^j)}{\lambda_+ - \lambda_-} + (1 - \delta_{i+1/2}^2) \frac{F_-^j + F_+^j}{2}, \quad (59)$$

where λ_\pm is for the characteristic speeds in the x -direction. $\delta_{i+1/2}$ is the newly introduced modification parameter, which is defined as

$$\delta_{i+1/2} = \tanh\left(\frac{1}{(\kappa_{\text{as}})_{i+1/2} \Delta x}\right); \quad (60)$$

where Δx is the grid width, and

$$(\kappa_{\text{as}})_{i+1/2} = \sqrt{(\kappa_a + \kappa_s)_i (\kappa_a + \kappa_s)_{i+1}} \quad (61)$$

is the total opacity at cell interface of index $i + 1/2$. In the optically thin region, the modification parameter $\delta \approx 1$ so that the modified flux (Equation (58)) reduces to the standard HLL flux. Conversely, the numerical dissipation term vanishes in the optically thick region as the modification parameter $\delta \ll 1$.

The characteristic speeds along the i direction are given by the interpolation of the characteristic speeds between the optically thin and thick limit (see Shibata et al. 2011)

$$\lambda_\pm^i = d_{\text{thin}} \lambda_{\pm, \text{thin}}^i + d_{\text{thick}} \lambda_{\pm, \text{thick}}^i; \quad (62)$$

where the characteristic speeds in the optically thin and thick limits are given by

$$\lambda_{\pm, \text{thin}}^i = -\beta^i \pm \alpha \frac{|\mathcal{F}^i|}{\sqrt{\mathcal{F}^i \mathcal{F}_i}}; \quad (63)$$

$$\lambda_{\pm, \text{thick}}^i = -\beta^i + \frac{2W^2 p^i \pm r}{2W^2 + 1}; \quad (64)$$

with $r \equiv \sqrt{\alpha^2 \gamma^{ii} (2W^2 + 1) - 2(Wp^i)^2}$; and $p^i \equiv \alpha v^i / W$. Note that, to prevent superluminal characteristic speed, Gmunu reconstructs $(\mathcal{E}, \mathcal{F}_i / \mathcal{E})$ instead of $(\mathcal{E}, \mathcal{F}_i)$ (O’Connor & Couch 2018b; Weih et al. 2020b).

3.5. Advection in Frequency-space

The computation of the fluxes in frequency-space f_ν (Equations (20) and (21)) requires the Eulerian decomposed variables of the third-rank moment $\mathcal{U}^{\mu\nu\rho}$, which can be obtained by (see Cardall et al. 2013; Mezzacappa et al. 2020)

$$\mathcal{W}^{\mu\nu\rho} = \gamma_\sigma^\mu \gamma_\kappa^\nu \gamma_\lambda^\rho \mathcal{U}^{\sigma\kappa\lambda}; \quad (65)$$

$$\mathcal{X}^{\mu\nu} = \frac{\mathcal{S}^{\mu\nu}}{W} + v_\rho \mathcal{W}^{\mu\nu\rho}; \quad (66)$$

$$\mathcal{Y}^\mu = \frac{\mathcal{F}^\mu}{W} + v_\nu \mathcal{X}^{\mu\nu}; \quad (67)$$

$$\mathcal{Z} = \frac{\mathcal{E}}{W} + v_\mu \mathcal{Y}^\mu = \alpha^3 \mathcal{U}^{\mu\mu}; \quad (68)$$

where the third-rank moment $\mathcal{U}^{\mu\nu\rho}$ can be obtained by Equation (3) with the fluid-frame moments $\{\mathcal{J}, \mathcal{H}^\mu, \mathcal{K}^{\mu\nu}, \mathcal{L}^{\mu\nu\rho}\}$.

Note that fluid accelerations (i.e., time-derivatives of the fluid velocities) involve the fluxes in frequency-space f_ν (Equations (20) and (21)). The terms that are proportional to the fluid accelerations are effectively of the order of $\mathcal{O}(v^2/c^2)$ in the radiation transport equations in the comoving frame (Buchler 1979; Kaneko et al. 1984; Munier & Weaver 1986; Lowrie et al. 2001; Rampp & Janka 2002; Just et al. 2015). The radiation transport equations in the comoving frame are correct up to the order of $\mathcal{O}(v/c)$ if these terms are ignored (Just et al. 2015; O’Connor & Couch 2018b; Skinner et al. 2019). In the current implementation, the time-derivatives of the Lorentz factor $\partial_t(W)$ and the velocities $\partial_t(Wv^i)$ are calculated simply by first-order backward differencing with the values of the previous time step, similar to O’Connor (2015). Adding these terms while preserving numerical stabilities is nontrivial; the proper treatment of these terms will be investigated in a future study.

Similar to the advection in space described in Section 3.4, the frequency advection term integrated with a frequency cell dV_ν at the f th frequency cell can be calculated by

$$\left[\int_{\Delta V_\nu} \frac{1}{\nu^2} \partial_\nu [\nu^2 f_\nu] dV_\nu \right]_f = [(\langle f_\nu \rangle \Delta A_\nu) |_{f+1/2} - (\langle f_\nu \rangle \Delta A_\nu) |_{f-1/2}], \quad (69)$$

where the cell surface area is given by Equation (42). As stated in Section 3.1, the advection term is integrated with the corresponding frequency-bin since Gmunu manipulates frequency-bin-integrated radiation quantities. Currently, Gmunu handles this energy advection term explicitly.

Since the fluxes in frequency-space f_ν can be expressed in terms of linear combinations of the fluid-frame radiation

momenta $\{\mathcal{J}, \mathcal{H}^\mu, \mathcal{K}^{\mu\nu}, \mathcal{L}^{\mu\nu\rho}\}$, the energy and momentum are conserved as long as the fluxes vanish at the outer boundary in the frequency-space. Similar to Müller et al. (2010), Kuroda et al. (2016), we split the flux as

$$\langle f_\nu \rangle_{\mathfrak{f}+1/2} \equiv \langle f_\nu \rangle_{\mathfrak{f}}^L + \langle f_\nu \rangle_{\mathfrak{f}+1}^R; \quad (70)$$

where we have defined

$$\langle f_\nu \rangle_{\mathfrak{f}}^L \equiv \langle f_\nu \rangle_{\mathfrak{f}} w_{\mathfrak{f}}; \quad (71)$$

$$\langle f_\nu \rangle_{\mathfrak{f}}^R \equiv \langle f_\nu \rangle_{\mathfrak{f}} (1 - w_{\mathfrak{f}}); \quad (72)$$

with the weighting function w

$$w_{\mathfrak{f}} \equiv \frac{j_{\mathfrak{f}+1/2}^\sigma}{j_{\mathfrak{f}-1/2}^\sigma + j_{\mathfrak{f}+1/2}^\sigma}. \quad (73)$$

Here, $j_{\mathfrak{f}+1/2}^\sigma$ is the weighted geometric mean of the distribution function j at cell interface $\mathfrak{f} + 1/2$, which is given by

$$j_{\mathfrak{f}+1/2}^\sigma \equiv \left[\left(\frac{\mathcal{J}_{\mathfrak{f}}}{\nu_{\mathfrak{f}}} \right)^{1-r_{\mathfrak{f}+1/2}} \left(\frac{\mathcal{J}_{\mathfrak{f}+1}}{\nu_{\mathfrak{f}+1}} \right)^{r_{\mathfrak{f}+1/2}} \right]^\sigma, \quad (74)$$

with $r_{\mathfrak{f}+1/2} \equiv (\nu_{\mathfrak{f}+1/2} - \bar{\nu}_{\mathfrak{f}}) / (\bar{\nu}_{\mathfrak{f}+1} - \bar{\nu}_{\mathfrak{f}})$, where $\bar{\nu}_{\mathfrak{f}}$ denotes the centroid of the \mathfrak{f} th cell. By default, we use a *harmonic* interpolation by setting $\sigma = 1$.

Note that, as discussed in Mezzacappa et al. (2020), this frequency-space advection approach has been developed in the context of *Lagrangian* two-moment schemes (Müller et al. 2010) to ensure neutrino number conservation. However, despite the fact that the fluxes in frequency-space f_ν can be expressed in terms of linear combinations of the fluid-frame radiation momenta $\{\mathcal{J}, \mathcal{H}^\mu, \mathcal{K}^{\mu\nu}, \mathcal{L}^{\mu\nu\rho}\}$ and the success in the frequency advection and application tests (see Sections 4.7 and 5.2 below; also see O'Connor 2015; Kuroda et al. 2016), it is still unclear whether the neutrino number conservation is still preserved (up to machine precision) if the same approach is applied directly to the Eulerian two-moment scheme as in O'Connor (2015), Kuroda et al. (2016). Further investigations and comparisons of different frequency advection schemes are needed, which will be left as future work.

3.6. Radiation–Fluid Interactions

The radiation–matter coupling source terms (Equation (7)) can be very large when the opacities are large. From the numerical point of view, these interaction source terms can become very stiff in the optically thick regime, and applying explicit time integration would be inefficient due to the extremely strict constraints on the time steps. IMEX Runge–Kutta schemes (e.g., Ascher et al. 1997; Pareschi & Russo 2005) offer an effective approach to overcome this challenge. These schemes have been applied and tested previously in *Gmnu* for resistive magnetohydrodynamics (Cheong et al. 2022), and also in several other radiation hydrodynamics codes (e.g., O'Connor 2015; Foucart et al. 2015; Kuroda et al. 2016; Weih et al. 2020b; Anninos & Fragile 2020; Radice et al. 2022; Izquierdo et al. 2023). For the details of the implementation of IMEX in *Gmnu*, we refer readers to our previous work (Cheong et al. 2022).

In general, most of the fluid conserved variables q_{hydro} have to be solved implicitly all together with the radiation moments (see, e.g., Kuroda et al. 2016). However, the computational cost is high because one will need to update the primitive variables

of fluid (such as pressure and specific energy) during the iteration when tabulated equations of state are being used. In this work, as in O'Connor (2015), Foucart et al. (2015), and Radice et al. (2022), we implicitly solve radiation moments $\{q_{\mathcal{E}}, q_{\mathcal{F}_i}\}$ only, and the coupling to the fluid is treated explicitly (see Section 3.6.2). Investigations of more-advanced fully implicit treatments such as Skinner et al. (2019), Laiu et al. (2021) are left as future work.

An implicit step that updates the solution of the radiation moments $\{q_{\mathcal{E}}, q_{\mathcal{F}_i}\}$ from the time step n (which is denoted as q^n) to the next time step $n + 1$ (which is denoted as q^{n+1}) can be expressed as

$$q^{n+1} = q^n + \Delta t_{\text{rad}}(q^{n+1}). \quad (75)$$

To obtain the updated solution q^{n+1} , we solve the nonlinear system $f(q)$, which is defined as

$$f(q) \equiv -q + q^n + \Delta t_{\text{rad}}(q). \quad (76)$$

Currently, we solve this nonlinear system by using a multidimensional Broyden method. The Jacobian $\partial f_i / \partial q_j$ of $f_i(q_j)$ is obtained numerically by forward differencing. The implementation of Broyden solver and computation of the Jacobian follows Press et al. (1996).

3.6.1. Initial Guess

A proper initial guess is needed for the implicit step. In this work, we follow the approach introduced by Radice et al. (2022). Although only monochromatic source terms (i.e., Equations (8) and (9)) are considered in this approach, we find that this method usually provides a good initial guess. For completeness, we describe the procedure of obtaining the initial guess at a given radiation frequency ν . First, we transform the solution q^n into fluid-frame, and denote it as $\{\tilde{\mathcal{J}}, \tilde{\mathcal{H}}_i\}$, and then update the fluid-frame moments by (see the *Lagrangian* two-moment model in Mezzacappa et al. 2020)

$$\hat{\mathcal{J}} = \tilde{\mathcal{J}} + \Delta t \frac{\alpha}{W} (\eta - \kappa_a \tilde{\mathcal{J}}); \quad (77)$$

$$\hat{\mathcal{H}}_i = \tilde{\mathcal{H}}_i - \Delta t \frac{\alpha}{W} (\kappa_a + \kappa_s) \tilde{\mathcal{H}}_i; \quad (78)$$

where $\hat{\mathcal{J}}$ and $\hat{\mathcal{H}}_i$ denote the updated fluid-frame moments. Second, we transform the updated $\hat{\mathcal{J}}$ and $\hat{\mathcal{H}}_i$ into the Eulerian-frame $\hat{\mathcal{E}}$ and $\hat{\mathcal{F}}_i$ by assuming optically thick

$$\hat{\mathcal{E}} = \frac{\hat{\mathcal{J}}}{3} (4W^2 - 1) - 2W \hat{\mathcal{H}}_{\alpha n^\alpha}; \quad (79)$$

$$\hat{\mathcal{F}}_i = W \hat{\mathcal{H}}_i + \left(\frac{4}{3} W^2 \hat{\mathcal{J}} - W \hat{\mathcal{H}}_{\alpha n^\alpha} \right) v_i; \quad (80)$$

where $\hat{\mathcal{H}}_0$ can be computed by the fact that $\hat{\mathcal{H}}_{\alpha} u^\alpha = 0$, and thus $\hat{\mathcal{H}}_{\alpha n^\alpha} = -\hat{\mathcal{H}}_i v^i$. The resulting Eulerian-frame moments $\hat{\mathcal{E}}$ and $\hat{\mathcal{F}}_i$ are used as the initial guess of the implicit step. Here, we assume the optically thick limit since the initial guess becomes important only in the optically thick regime.

Note that, as discussed in Radice et al. (2022), the updated $\hat{\mathcal{J}}$ and $\hat{\mathcal{H}}_i$ are exact solutions only at the leading order in v/c where $u^\mu \partial_\mu \approx W \partial_t$ and when only monochromatic source terms are considered. However, the corresponding Eulerian-frame moments $\hat{\mathcal{E}}$ and $\hat{\mathcal{F}}_i$ are not correct solutions even if the closure is taken into account during the transformation.

3.6.2. Coupling to Fluid

Once the radiation moments are solved, we explicitly update the fluid's energy and momentum by

$$q_{\tau} \rightarrow q_{\tau} - \Delta t \sum_{\text{species}} \int s_{\text{rad}\mathcal{E}} dV_{\nu}, \quad (81)$$

$$q_{S_i} \rightarrow q_{S_i} - \Delta t \sum_{\text{species}} \int s_{\text{rad}\mathcal{F}_i} dV_{\nu}, \quad (82)$$

where $s_{\text{rad}\mathcal{E}}$ and $s_{\text{rad}\mathcal{F}_i}$ are obtained by Equations (26) and (27) with the updated radiation moments.

3.6.3. Rank of Nonlinear System

In general, a nonlinear system of dimensions $(N_{\text{dim}} + 1) \times N_{\nu} \times N_{\text{species}}$ must be solved. Here we assume the fluid quantities are kept fixed during the implicit step and consider N_{ν} frequency-bins, N_{species} species of neutrino, in N_{dim} dimensional spatial space. Since the size of the nonlinear system could be very large, it is computationally expensive if we fully solve this system. In practice, depending on the nature of the problem, it is not necessary to apply the full implicit solver. Avoiding full implicit treatment would significantly reduce the computational cost. Similar to Just et al. (2015), we list different modes of the radiation-interaction source terms' treatment, which are implemented in Gmunu:

1. *Multispecies multigroup.* All radiation moments $\{q_{\mathcal{E}}, q_{\mathcal{F}_i}\}$ are solved fully implicitly. This is the general mode discussed above, where the dimensions of the nonlinear system is $(N_{\text{dim}} + 1) \times N_{\nu} \times N_{\text{species}}$.
2. *Single-species multigroup.* The radiation moments $\{q_{\mathcal{E}}, q_{\mathcal{F}_i}\}$ are solved for each species separately. The dimensions of the nonlinear system now reduced to N_{species} nonlinear systems of dimensions $(N_{\text{dim}} + 1) \times N_{\nu}$. Since the source terms that contain species coupling are treated explicitly in this mode, this mode is less accurate when the species coupling is strong.
3. *Single-species single-group.* The radiation moments $\{q_{\mathcal{E}}, q_{\mathcal{F}_i}\}$ are solved for each species and for each frequency-group separately. The dimensions of the nonlinear system now reduced to $N_{\text{species}} \times N_{\nu}$ nonlinear systems of dimensions $(N_{\text{dim}} + 1)$. Since this mode is purely monochromatic, the coupling of a different frequency-group cannot be done implicitly. In this mode, only the emission and/or absorption and elastic scattering source terms ($S_{\text{E/A}}^{\mu}$ and S_{ES}^{μ} , see Equations (8) and (9)) are solved implicitly, while the source terms that contain species or frequency couplings are treated explicitly. In this case, we have included the analytic Jacobian for implicit solver by following Radice et al. (2022). The details of which can be found in Appendix A.

In practice, to minimize the computational cost, we switch to different modes in different stages of the simulations, where the criteria of which are highly problem dependent.

3.7. Transformation from Eulerian-frame to Fluid-frame

As shown in the previous sections, although the radiation fields are solved in the Eulerian-frame, the radiation moments in the fluid-frame are often needed in most of the calculations. The most straightforward way to compute the fluid-frame moments $\{\mathcal{J}, \mathcal{H}^{\mu}\}$ is to contract the energy-momentum tensor

$T^{\mu\nu}$ with the comoving four-velocities u^{μ} . Alternatively, we found it is useful to directly express the fluid-frame moments $\{\mathcal{J}, \mathcal{H}^{\mu}\}$ in terms of the Eulerian-frame moments $\{\mathcal{E}, \mathcal{F}^{\mu}\}$, especially when only part of the fluid-frame moments is needed. We decompose $\{\mathcal{J}, \mathcal{H}^{\mu}, \mathcal{H}^{\mu}\mathcal{H}_{\mu}\}$ and express them in terms of the Eulerian-frame moments $\{\mathcal{E}, \mathcal{F}^{\mu}\}$ by following Deppe et al. (2022), Radice et al. (2022). The details of which can be found in Appendix B.

3.8. Enforcing Validity

Unphysical solutions occasionally arise during the evolution due to the numerical round-off errors especially when the radiation energy density \mathcal{E} is very small. In Gmunu, we include the following error handling policies to enforce the validity of the numerical solution.

Similar to the standard ‘‘atmosphere’’ treatment for rest-mass density ρ in hydrodynamical simulation (e.g., Cheong et al. 2020, 2021), we enforce the nonnegativity of the energy density \mathcal{E} . In particular, we define a minimum allowed distribution function f_{min} and a threshold f_{thr} , where $f_{\text{thr}} \geq f_{\text{min}} \geq 0$. Whenever the energy density drops below the threshold (i.e., when $\mathcal{E}(\nu) < \nu f_{\text{thr}}$), we set the energy to be the minimum allowed energy density νf_{min} , and enforce a vanishing flux by setting $\mathcal{F}_i(\nu) = 0$. In the gray transport cases, f_{min} and f_{thr} represent the minimum allowed energy density and the threshold directly.

In addition to the negative energy density, unphysical solutions could also arise when $\mathcal{F}^i \mathcal{F}_i > \mathcal{E}^2$. Similar to Kuroda et al. (2016), Rivera-Paleo & Guzmán (2019), we enforce

$$\mathcal{F}_i \rightarrow \mathcal{F}_i \times \min(\xi_{\text{max}}, \xi_{\text{max}}/\xi), \quad (83)$$

where we have defined the Eulerian flux factor

$$\xi \equiv \sqrt{\mathcal{F}^i \mathcal{F}_i / \mathcal{E}^2}, \quad (84)$$

and ξ_{max} is the maximum allowed Eulerian flux factor. Unless explicitly stated, we set $f_{\text{thr}} = 10^{-30}$, $f_{\text{min}} = 0$, and $\xi_{\text{max}} = 1$.

4. Numerical Tests

In this section, we present a selection of representative test problems with our code to assess the performance and accuracy of our new two-moment-based module. The tests range from special-relativistic to general-relativistic radiation transfer, from one to multiple dimensions, and from frequency-integrated (gray) to multifrequency group. Here, we consider only the monochromatic source terms (i.e., at a given radiation frequency ν , the calculation of the radiation emissivity, absorption, and scattering coefficients $\eta(\nu)$, $\kappa_a(\nu)$, and $\kappa_s(\nu)$ do not depend on other radiation frequencies $\nu' \neq \nu$; see Equations (8) and (9)) with idealized opacities. Tests with sophisticated realistic neutrino opacities are presented in Section 5.

For the frequency-integrated (gray) test, we denote the frequency-integrated radiation energy and momentum in the fluid-frame as

$$J = \int_0^{\infty} \mathcal{J} dV_{\nu}; H_i = \int_0^{\infty} \mathcal{H}_i dV_{\nu}, \quad (85)$$

and so as the case for the fluid-frame moments

$$E = \int_0^{\infty} \mathcal{E} dV_{\nu}; F_i = \int_0^{\infty} \mathcal{F}_i dV_{\nu}. \quad (86)$$

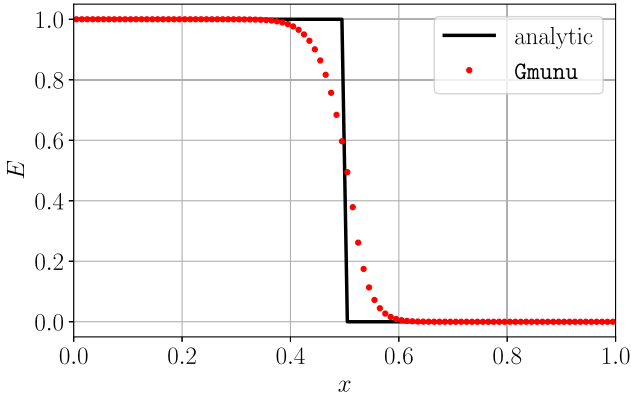


Figure 1. The energy density profile of the radiation E at $t = 1$, where the radiation has propagated through the velocity jump at $x = 0$. Despite the discontinuity of the velocity profile, the numerical solution obtained by Gmunu does not have artificial oscillations at the velocity jump interface $x = 0$, or at the radiation front $x = 0.5$.

In addition, we denote the frequency-integrated emissivity η , energy-averaged absorption and scattering coefficients as

$$\bar{\eta} = \int_0^\infty \eta dV_\nu, \quad (87)$$

$$\bar{\kappa}_a = \frac{\int_0^\infty \kappa_a \nu f dV_\nu}{\int_0^\infty \nu f dV_\nu}, \quad (88)$$

$$\bar{\kappa}_s = \frac{\int_0^\infty \kappa_s \nu f dV_\nu}{\int_0^\infty \nu f dV_\nu}, \quad (89)$$

where f is the distribution function. Unless otherwise specified, all simulations reported in this paper were performed with HLL Riemann solver Harten et al. (1983), second-order Minmod limiter Roe (1986) with IMEX-SSP2(2,2,2) time integrator Pareschi & Russo (2005).

4.1. Transparent Fluid with a Velocity Jump

In this section, we consider the propagation of radiation in a moving optically thin medium as in Radice et al. (2022). In particular, we consider a 1D mildly relativistic fluid moving with Lorentz factor $W = 2$ in an opposite direction in a flat spacetime. The background fluid velocity profile is chosen to be

$$W_V^x = \begin{cases} \sqrt{W^2 - 1}, & \text{if } x > 0 \\ -\sqrt{W^2 - 1}, & \text{otherwise} \end{cases}. \quad (90)$$

The initial profile of the radiation is set to be

$$E = \begin{cases} 1, & \text{if } x < -0.5 \\ 0, & \text{otherwise} \end{cases}, \quad (91)$$

and $F_x = E$. To consider the case in an optically thin limit, we consider zero opacities, i.e., $\bar{\eta} = \bar{\kappa}_s = \bar{\kappa}_a = 0$. In this test, the hydrodynamical profiles are kept fixed, and disable the interaction between the fluid and radiation during the evolution. We assume slab geometry, and the computational domain covers the region $[-1, 1]$ with 200 grid points.

Figure 1 shows the energy density profile of the radiation E at $t = 1$, where the radiation has propagated through the velocity jump at $x = 0$. Despite the discontinuity of the velocity

profile, the numerical solution obtained by Gmunu has artificial oscillations neither at the velocity jump interface $x = 0$; nor at the radiation front $x = 0.5$. This test demonstrates that Gmunu is able to handle the radiation transport in a mildly relativistic moving fluid.

4.2. Homogeneous Radiating Sphere

The homogeneous radiating sphere test is a toy model of a hot neutron star, which emits neutrinos. As discussed in Smit et al. (1997), O'Connor (2015), Murchikova et al. (2017), and Anninos & Fragile (2020), this test is sensitive to the chosen closure relation. In this test, we consider a homogeneous sphere with a radius R with constant emission, and absorption rate $\bar{\eta} = \bar{\kappa}_a$, and simply ignore scatterings ($\bar{\kappa}_s = 0$). As discussed in Smit et al. (1997), this problem has an analytic solution

$$I(r, \mu) = B \{1 - \exp[-\bar{\kappa}_s(r, \mu)]\}, \quad (92)$$

where B is the strength of the initial energy density of the radiation,

$$s(r, \mu) = \begin{cases} r\mu + Rg(r, \mu) & \text{if } r < R \text{ and } -1 \leq \mu \leq 1, \\ 2Rg(r, \mu) & \text{if } r \geq R \text{ and } \sqrt{1 - \left(\frac{R}{r}\right)^2} \leq \mu \leq 1, \\ 0 & \text{otherwise,} \end{cases} \quad (93)$$

and

$$g(r, \mu) = \sqrt{1 - \left(\frac{r}{R}\right)^2} (1 - \mu^2), \quad (94)$$

in which $\mu \equiv \cos \theta$ is the directional cosine. The analytic solutions for J and H are

$$\{J, H\} = \frac{1}{2} \int_{-1}^1 d\mu \mu^{(0,1)} I. \quad (95)$$

Note that when the background velocities are zero, the radiation moments in the fluid-frame are the same as in Eulerian-frame.

We simulate this problem by setting the radius of the sphere R and the strength of the initial energy density of the radiation B to be unity (i.e., $R = 1 = B$). The initial profile of the radiation is set to be

$$(E, F_r/E) = \begin{cases} (B, 0) & \text{if } r < R, \\ \left(B \left(\frac{R^2}{r^2}\right), 0.1\right) & \text{otherwise.} \end{cases} \quad (96)$$

The hydrodynamical profiles are kept fixed, and disable the interaction between the fluid and radiation during the evolution. To see how our code behaves with different opacities in this test, we perform the test with three different absorption opacities: $\bar{\kappa}_a = 10^6, 10, 1$, respectively. Although this is a spherically symmetric test problem, which can be run in 1D spherical coordinates (e.g., O'Connor 2015), we simulated this problem in 1D Cartesian coordinates (x, y, z) to minimize the symmetry imposed in the simulation. In particular, the computational domain covers the region $[-5, 5] \times [-5, 5] \times [-5, 5]$ with the resolution 256^3 .

Figure 2 compares the energy density E and the radial flux ratios F_r/E along x -axis at $t = 10$ with the analytic solutions.

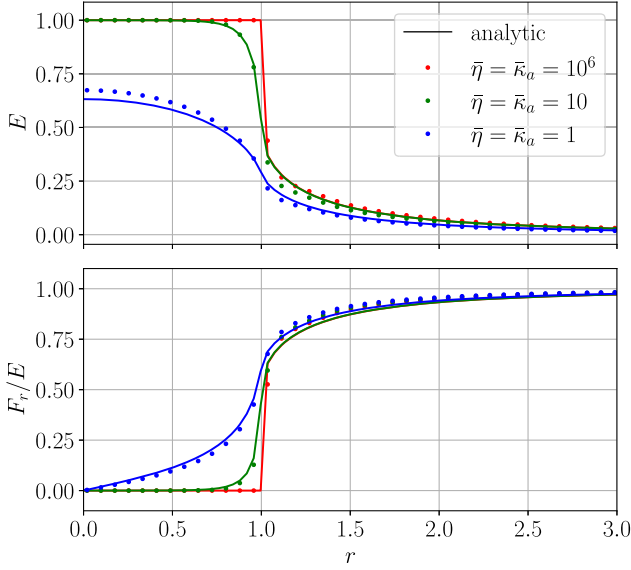


Figure 2. Energy density E (upper panel) and the radial flux ratios F_r/E (lower panel) along x -axis at time $t = 10$ of the homogeneous radiation sphere test. Since the profiles are extracted along the x -axis, the x coordinate has the same value of radius r . The dots show the numerical results obtained by Gmunu while the solid lines show the corresponding analytic solution. For the high opacity cases (i.e., $\bar{\kappa}_a \geq 10$, the red and green dots), the numerical results are mostly indistinguishable from the reference solution except the region nearby the discontinuity at the surface of the sphere. However, for the low-opacity case ($\bar{\kappa}_a = 1$, the blue dots), the numerical results of the energy density E are less accurate inside the sphere. This is because the analytic closure does not give the correct second moment in the intermediate opacities regime (i.e., $\kappa \lesssim 1$).

For the high-opacity cases (i.e., $\bar{\kappa}_a \geq 10$, the red and green dots), Gmunu resolves the optically thick and thin region well despite the discontinuities at the surface of the sphere. While the analytic closure gives the correct second moment in the high-opacity regime and the free-streaming regime, this is not the case for the intermediate regime (e.g., for the region where the opacity $\kappa \lesssim 1$) (Murchikova et al. 2017; Weih et al. 2020b). As a result, for the low-opacity ($\bar{\kappa}_a = 1$, blue dots) case, the numerical results of the energy density E inside the sphere are less accurate while the exterior energy density tail still matches the analytic results. A similar feature has also been seen in Weih et al. (2020b).

4.3. Diffusive Limit in a Scattering Medium

In this test, we consider the diffusion of radiation when the scattering opacity is high, and the mean free path is small compare to the grid size Δx (e.g., Radice et al. 2022; Izquierdo et al. 2023). The initial profile of the radiation is set to be

$$E = \theta\left(x + \frac{1}{2}\right) - \theta\left(x - \frac{1}{2}\right), \quad (97)$$

where $\theta(x)$ is the Heaviside step function, and $F^i = 0$. We consider this diffusion in a purely scattering medium; we set $\bar{\eta} = 0 = \bar{\kappa}_a$, and $\bar{\kappa}_s = 10^3$. Here, we again consider static background hydrodynamical profiles, and assume slab geometry. The computational domain covers the region $[-2, 2]$ with 256 grid points.

The evolution of the energy density E can be approximated by the diffusion equation $\partial_t E = (\partial_x^2 E)/3\kappa_s$ when the time-scales are longer than the equilibrium time (Radice et al. 2022;

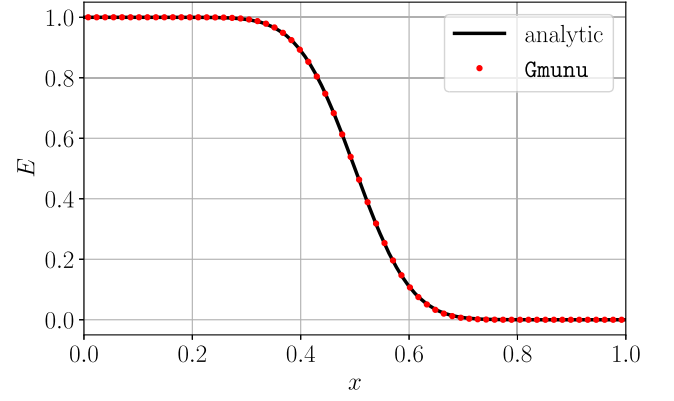


Figure 3. The energy density profile of the radiation E at $t = 10$ in a purely scattering medium, with high scattering opacity $\bar{\kappa}_s = 10^3$. The red dots show the numerical solution obtained by Gmunu while the black solid line shows the reference analytic solution from Equation (98) in the diffusive limit. This indicates that Gmunu captures correct diffusion rate even in diffusive limit.

Izquierdo et al. 2023). The exact solution of which is given by

$$E(t, x) = \frac{1}{2} \left[\operatorname{erf}\left(\frac{x + \frac{1}{2}}{\sqrt{4\tau t}}\right) - \operatorname{erf}\left(\frac{x - \frac{1}{2}}{\sqrt{4\tau t}}\right) \right], \quad (98)$$

where $\tau = 1/(3\kappa_s)$ is the diffusion timescale.

Figure 3 shows the energy density profile of the radiation E at time $t = 10$. As shown in the figure, the numerical solution obtained by Gmunu (red dots) agrees with the reference analytic solution from Equation (98) in the diffusive limit (black solid line). This demonstrates that Gmunu is able to capture a correct diffusion rate even when the scattering opacity is high.

To quantify the convergence rate at $t = T \equiv 10$, we perform the simulation with different resolutions, and compute the L_1 -norm of the difference between the exact and final ($t = 10$) values of the energy density of the radiation E as

$$\|E(T) - E_{\text{exact}}(T)\|_1 \equiv \frac{\sum_i |E(T) - E_{\text{exact}}(T)| \Delta V_i}{\sum_i \Delta V_i}; \quad (99)$$

Figure 4 shows the L_1 -norm of the difference between the exact and final ($t = 10$) values of the energy density of the radiation E . The order of convergence of this test is roughly 1.86.

4.4. Diffusive Limit in a Moving Medium

In this test, we consider a propagation of a radiation in a moving purely scattering medium as in Radice et al. (2022), Izquierdo et al. (2023). This is known to be a demanding test so that the result is highly sensitive to the implicit treatment (Radice et al. 2022). Consider a Gaussian pulse of radiation

$$E = \exp(-9x^2), \quad (100)$$

which is fully trapped ($H^\mu = 0$) in the medium. The radiation flux in Euler frame can be written as

$$F_i = \frac{4}{3} J W^2 v_i, \quad (101)$$

where $J = 3E/(4W^2 - 1)$ in this case. The medium is set to be purely scattering (i.e., $\bar{\eta} = 0 = \bar{\kappa}_a$) with high scattering opacity $\bar{\kappa}_s = 10^3$, which moves with a relativistic velocity $v^x = 0.5$.

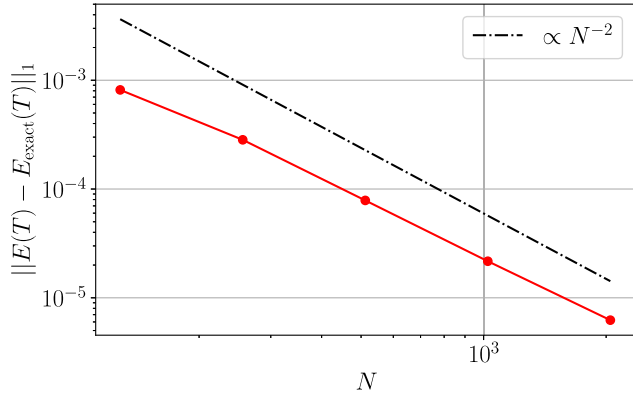


Figure 4. The L_1 -norm of the difference between the exact and final ($t = 10$) values of the energy density of the radiation E at different resolution N . The second-order ideal scaling is given by the black dashed line. In this test, second-order, accurate strong-stability-preserving IMEX-SSP2(2,2,2) time integrator from Pareschi & Russo (2005), the Harten, Lax, and van Leer Riemann solver from Harten et al. (1983), and a second-order solver from Minmod limiter Roe (1986) are used. The code achieves roughly 1.86 order of convergence in this test.

Here, we assume slab geometry, and the computational domain covers the region $[-5, 5]$ with 1024 grid points.

Figure 5 shows the radiation energy density profile at time $t = 4$. As shown in the figure, the results obtained by using Gmumu agree with the semianalytic reference solution.

4.5. Diffusive Point Source

Here, we present a test, which also focuses on the scattering regime, i.e., the diffusive point-source test proposed by Pons et al. (2000). This test describes the evolution of a single point source in the diffusive limit. The initial condition, and also the analytic solution, is given by

$$E(r, t) = \left(\frac{\bar{\kappa}_s}{t}\right)^{N_{\text{dim}}/2} \exp\left(\frac{-3\bar{\kappa}_s r^2}{4ct}\right), \quad (102)$$

$$F^r(r, t) = \frac{r}{2t} E(r, t), \quad (103)$$

where N_{dim} is the number of dimensions, which is set to be 2. In this test, we consider a purely scattering medium with a scattering opacity $\bar{\kappa}_s = 100$. The simulation starts from $t = 1$, to $t = 4$. We assume cylindrical geometry in 1D, and the computational domain covers the region $[0, 1]$ with 128 grid points.

Figure 6 compares the energy density E at different time t to the analytic solution. Because the simulation starts from $t = 1$, the Gmumu result is identical to the analytic solution. As shown in the figure, the Gmumu result agrees with the analytic solution.

4.6. Shadow Casting Problems

Here we present multidimensional tests, which describe the interaction between radiation and a cylinder with high absorption opacity.

First, we consider a radiation beam propagating from left to right. The initial condition is given as

$$E = \begin{cases} 1, & \text{if } x \leq -0.4 \text{ and } y \in [-0.12, 0.12]; \\ 10^{-16}, & \text{otherwise,} \end{cases} \quad (104)$$

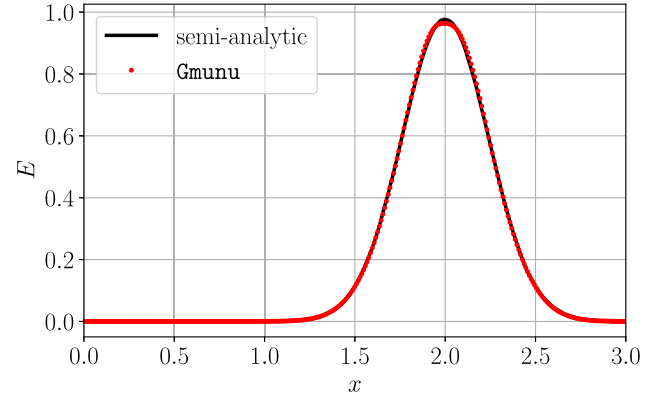


Figure 5. The energy density profile of the radiation E at $t = 4$ in a purely scattering medium, with high scattering opacity $\bar{\kappa}_s = 10^3$, which moves with a relativistic velocity $v^x = 0.5$. The red dots show the numerical solution obtained by Gmumu while the black solid line shows the corresponding semianalytic solution. Note that this is known to be a demanding test, in the sense that the result is highly sensitive to the treatment of the optically thick limit (Radice et al. 2022). This figure shows that the results returned by Gmumu agree with the semianalytic solution.

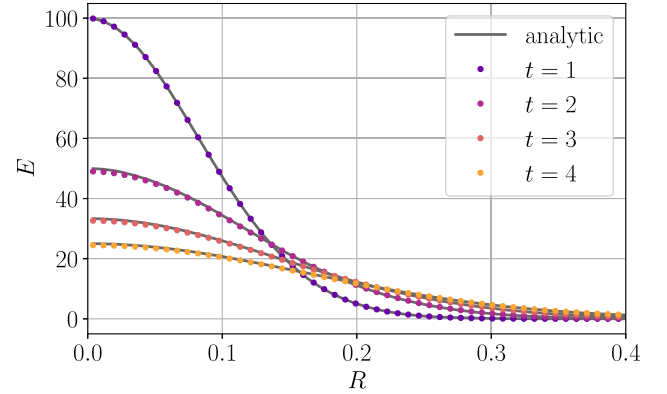


Figure 6. Comparison of the energy density profile E at time $t = 1, 2, 3, 4$ to the analytic solution (gray solid lines). Since the simulation starts from $t = 1$, the result is identical to the analytic solution. As shown in the figure, results produced by utilizing Gmumu agree with the analytic solution.

and we set $(F_x/E, F_y/E, F_z/E) = (0.999999, 0, 0)$ everywhere in the computational domain. In this test, we consider a cylinder of radius $R = 0.07$, and located at $(-0.2, 0)$ with an extremely high absorption coefficient, $\bar{\kappa}_a = 10^6$. This initial condition is kept fixed during the entire evolution for $x \leq -0.4$. Note that this high absorption opacity $\bar{\kappa}_a$ is around 6 orders of magnitude larger than the radiation moments, resulting in significantly stiff interaction source terms in the evolution equations. We choose this stiff situation on purpose to challenge the nonlinear implicit solver and the IMEX time integrator implemented in Gmumu. This test is run with a uniform grid 256×128 , which covers the region $[-0.5, 0.5]$ for x and $[-0.25, 0.25]$ for y .

Figure 7 shows the radiation energy density profile at $t = 1$. As shown in the figure, the radiation beam propagates from left to right, and is obstructed by the optically thick cylinder. This results in a shadow behind the cylinder, and a split for the beam into two parts, which keep propagating to the right.

Shadow casting tests have been carried out in more nontrivial geometries by considering a point source (Just et al. 2015; Kuroda et al. 2016; O'Connor & Couch 2018b). Similar to Just et al. (2015), Kuroda et al. (2016), and

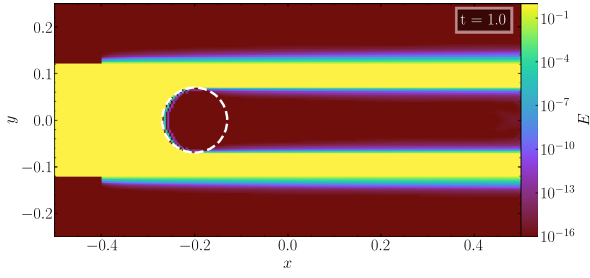


Figure 7. The radiation energy density profile at $t=1$, where the initial conditions are kept fixed for $x \leq -0.4$ during the entire evolution. The radiation beam propagates from left to right, and is blocked by the optically thick cylinder (white dashed line) with high absorption opacity $\bar{\kappa}_a = 10^6$. As a result, this cylinder split the beam into two. The two beams keep propagating to the right, and a shadow is cast behind the cylinder.

O’Connor & Couch (2018b), here we consider a point source, which is located at the origin $r=0$, with the radius $r_{\text{src}}=1.5$. The source has the absorption opacity

$$\kappa_a = 10 \exp[-(4r/r_{\text{src}})^2], \quad (105)$$

and emissivity $\eta = \kappa_a J_{\text{eq}}$, where we choose $J_{\text{eq}} = 1$. In addition, we also consider a purely absorbing sphere ($\bar{\eta} = 0 = \bar{\kappa}_s$), with radius $r_{\text{shadow}} = 2$, located at a distance of $d = 8$ from the center of the source. Unlike Just et al. (2015), Kuroda et al. (2016), and O’Connor & Couch (2018b), here we consider a high absorption opacity $\kappa_a = 10^6$ for the sphere. To make the setup slightly asymmetric along the $x-y$ plane, instead of placing the absorbing sphere at the equatorial plane, we place it at the polar angle $\theta = 11\pi/24$ (i.e., the z coordinate of the center of the absorbing sphere is $d \cos(\theta)$). This test is run in the cylindrical coordinate (R, z) with a uniform grid 128×128 , which covers the region $[0, 12]$ for R and $[-6, 6]$ for z .

Figure 8 shows the radiation energy density profile scaled with r^2 at $t=5, 10, 15$, respectively. The scaling of r^2 is to achieve a mostly constant value in the free-streaming regime (O’Connor & Couch 2018b). Similar to the single beam case discussed above (see Figure 7), this sphere absorbs radiation and produces a shadow. This indicates that our code behaves well in this test despite that in the 2D cylindrical coordinate with an off-angle setup.

4.7. Gravitational Redshift and Doppler Shift

The tests presented above are all frequency-integrated tests. To test if the code handles the energy-coupling terms for gravitational redshift and Doppler shift (see Section 3.5) correctly, we perform the test introduced by Müller et al. (2010), which has been used as a branch mark test by several authors, e.g., O’Connor (2015), Kuroda et al. (2016), Anninos & Fragile (2020), and Chan & Müller (2020).

To separately assess the handling of Doppler shift (with nonzero velocity profile), gravitational redshift (with curved spacetime), and the combination of these two, we mainly follow the setup in Müller et al. (2010). In particular, we consider a sphere with radius $R = 10$ km, with a uniform density $\rho = 9 \times 10^{14} \text{g cm}^{-3}$. In addition, we consider a sharp velocity profile, which mimics the accretion phase of core-

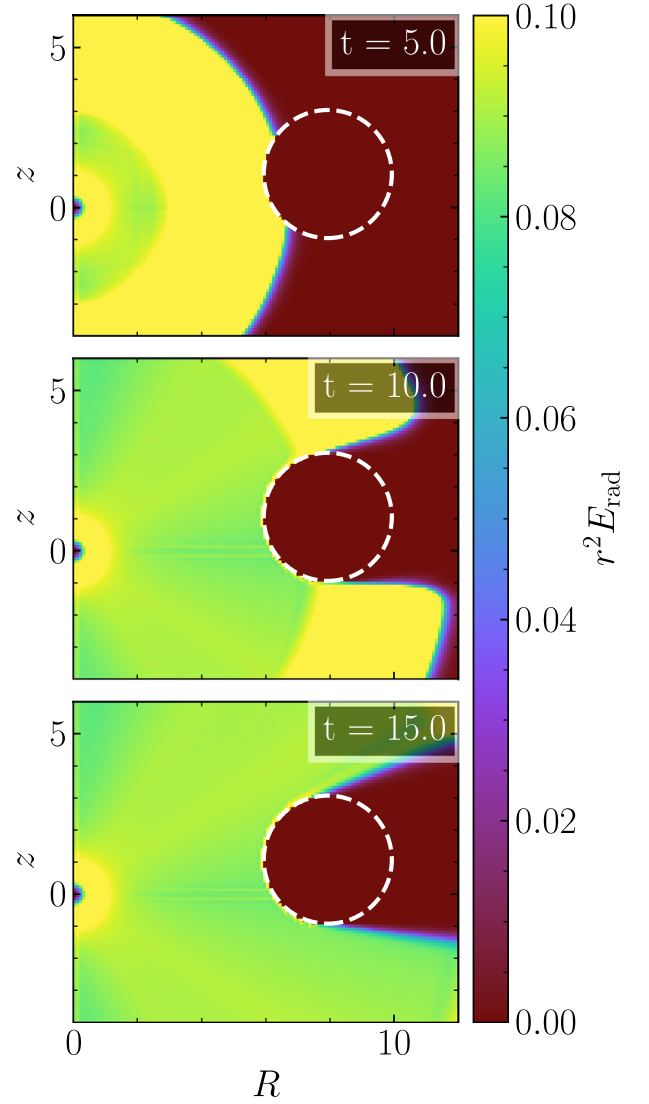


Figure 8. The radiation energy density profile scaled with r^2 at different time slides. The radiation propagates spherically from the source to outside, and is blocked by the optically thick sphere (white dashed line) with high absorption opacity $\bar{\kappa}_a = 10^6$. As in the single beam case (see Figure 7), this sphere absorbs radiations and causes a shadow behind it.

collapse supernovae

$$v_r = \begin{cases} 0, & \text{if } r \leq 135 \text{ km;} \\ -0.2c \left(\frac{r - 135 \text{ km}}{150 \text{ km} - 135 \text{ km}} \right), & \text{if } 135 \text{ km} < r \leq 150 \text{ km;} \\ -0.2c \left(\frac{150 \text{ km}}{r} \right)^2, & \text{if } r > 150 \text{ km.} \end{cases} \quad (106)$$

Given the rest-mass density and velocity profiles, the metric quantities such as the conformal factor ψ , the lapse function α , and the shift vector β^i are calculated by utilizing the metric solver in Gmunu (Cheong et al. 2020, 2021). The initial neutrino profile is set as follows:

$$(\mathcal{E}, \mathcal{F}_r/\mathcal{E}) = \begin{cases} (\mathcal{B}, 10^{-2}) & \text{if } r \leq R; \\ \left(\mathcal{B} \left(\frac{R}{r} \right)^2, 1 - 10^{-3} \right) & \text{if } r > R, \end{cases} \quad (107)$$

where \mathcal{B} is the blackbody function, which is a function of frequency ν , chemical potential μ , and temperature T . Specifically, under the chosen convention, the blackbody function is given by

$$\mathcal{B}(\nu, \mu, T) = \frac{\nu}{\exp[(h\nu - \mu)/k_B T] + 1}, \quad (108)$$

where h is Planck's constant, and k_B is Boltzmann's constant. In this test, the chemical potential is chosen to be $\mu = 0$, and the temperature is set to be $T = 5$ MeV. The absorption coefficient κ_a is set to be 60 cm^{-1} in the sphere ($r \leq R$) while vanishing elsewhere. The emissivity is simply $\eta = \kappa_a \mathcal{B}$. In this test, we consider spherical coordinate in 1D. The computational domain covers $[0, 10^4]$ km for r , with the resolution $N_r = 128$ and allowing 6 mesh levels (an effective resolution of 4096). The refinement level is decided by a ratio $\Delta r/r$. In particular, we refine the block if $\Delta r/r > 0.01$ in any of the grid in the block. The frequency-space is discretized into 18 groups logarithmically from 1 to 280 MeV/ h . The simulation is performed until the system reaches a stationary state; the results are extracted at $t_{\text{max}} = 1$ s.

As discussed in Müller et al. (2010), a stationary solution is available for this test. In particular, the average neutrino energy $\langle \varepsilon \rangle$ and the redshift-corrected luminosity L_{rs} obey the following relations:

$$W\alpha(1 + v_r)\langle \varepsilon \rangle = \text{constant}; \quad (109)$$

$$\frac{1 + v_r}{1 - v_r} L_{\text{rs}} = \text{constant}; \quad (110)$$

where W is the Lorentz factor. The average neutrino energy and the redshift-corrected luminosity are defined as

$$\langle \varepsilon \rangle = \frac{\int_0^\infty \mathcal{J} dV_\nu}{\int_0^\infty \mathcal{J} / \nu dV_\nu}, \quad \text{and} \quad (111)$$

$$L_{\text{rs}} = 4\pi r^2 \alpha^2 \psi^4 \int_0^\infty \mathcal{H} dV_\nu, \quad (112)$$

respectively. In the following, the analytic solution is computed based on the value at the surface of the sphere, i.e., $\langle \varepsilon \rangle(r = R)$, and $L_{\text{rs}}(r = R)$. In addition, the numerical results are scaled by their corresponding value at the outer boundary of the computational domain, i.e., $\langle \varepsilon \rangle_\infty \equiv \langle \varepsilon \rangle(r = 10^4 \text{ km})$, and $L_{\text{rs},\infty} \equiv L_{\text{rs}}(r = 10^4 \text{ km})$.

Figure 9 compares the rescaled average neutrino energy $\langle \varepsilon \rangle / \langle \varepsilon \rangle_\infty$ and the redshift-corrected luminosity $L_{\text{rs}} / L_{\text{rs},\infty}$ obtained by utilizing Gmunu (red dots) and the analytic solutions (black solid lines). As in Müller et al. (2010), we consider three cases: namely, (i) the shape velocity profile in flat spacetime (left column); (ii) vanishing velocities in curved spacetime (middle column); and (iii) the shape velocity profile in curved spacetime (right column). The numerical results obtained by Gmunu agree with the analytic results well in all three cases. This test demonstrates that Gmunu is able to handle the advection terms in the frequency-space, which corresponds to gravitational redshift and Doppler shift affects of the radiation with different frequencies.

5. Application Examples

The tests presented in the previous section considered only the monochromatic radiation source terms (i.e., there are no species or frequency couplings) and with idealized opacities. To test if our code is able to handle the radiation where different species and frequencies are strongly coupled, in this section, we consider the neutrino transport in the context of core-collapse supernovae and hot neutron star as examples.

5.1. Neutrino Source Terms and Couplings

In addition to the source terms of emission, absorption, and elastic scattering, our application examples also incorporate the source terms of neutrino–lepton inelastic scattering, denoted as $\mathcal{S}_{\text{IS}}^\mu$, and neutrino-pair processes, denoted as $\mathcal{S}_{\text{Pair}}^\mu$. These terms describe the neutrino–electron inelastic scattering and electron–positron pair annihilation. In this case, the radiation four-force for neutrinos can be written as (Shibata et al. 2011; O'Connor 2015)

$$\mathcal{S}_{\text{rad}}^\mu = \mathcal{S}_{\text{E/A}}^\mu + \mathcal{S}_{\text{ES}}^\mu + \mathcal{S}_{\text{IS}}^\mu + \mathcal{S}_{\text{Pair}}^\mu; \quad (113)$$

where, for each species, the inelastic scattering $\mathcal{S}_{\text{IS}}^\mu$ and the neutrino-pair processes $\mathcal{S}_{\text{Pair}}^\mu$ terms are defined as

$$\begin{aligned} \mathcal{S}_{\text{IS}}^\mu(\nu) = & \int \frac{dV_{\nu'}}{\nu'} \{ [\nu - \mathcal{J}(\nu)] u^\mu - \mathcal{H}^\mu(\nu) \} \mathcal{J}(\nu') R_0^{\text{in}}(\nu, \nu') \\ & + \frac{\mathcal{H}^\mu(\nu')}{3} \{ [\nu - \mathcal{J}(\nu)] R_1^{\text{in}}(\nu, \nu') + \mathcal{J}(\nu) R_1^{\text{out}}(\nu, \nu') \} \\ & - \{ h_{\alpha\beta} \mathcal{H}^\alpha(\nu) \mathcal{H}^\beta(\nu') u^\mu + \tilde{\mathcal{K}}^{\mu\alpha}(\nu) \mathcal{H}_\alpha(\nu') \} \\ & \times [R_1^{\text{in}}(\nu, \nu') - R_1^{\text{out}}(\nu, \nu')] \\ & - [\mathcal{J}(\nu) u^\mu + \mathcal{H}^\mu(\nu)] [\nu' - \mathcal{J}(\nu')] R_0^{\text{out}}(\nu, \nu'); \end{aligned} \quad (114)$$

$$\begin{aligned} \mathcal{S}_{\text{Pair}}^\mu(\nu) = & \int \frac{dV_{\nu'}}{\nu'} \{ [\nu - \mathcal{J}(\nu)] u^\mu - \mathcal{H}^\mu(\nu) \} [\nu' - \tilde{\mathcal{J}}(\nu')] R_0^{\text{pro}}(\nu, \nu') \\ & - \frac{\tilde{\mathcal{H}}^\mu(\nu')}{3} \{ [\nu - \mathcal{J}(\nu)] R_1^{\text{pro}}(\nu, \nu') + \mathcal{J}(\nu) R_1^{\text{ann}}(\nu, \nu') \} \\ & + \{ h_{\alpha\beta} \mathcal{H}^\alpha(\nu) \tilde{\mathcal{H}}^\beta(\nu') u^\mu + \tilde{\mathcal{K}}(\nu)^{\mu\alpha} \tilde{\mathcal{H}}_\alpha(\nu') \} \\ & \times [R_1^{\text{pro}}(\nu, \nu') - R_1^{\text{ann}}(\nu, \nu')] \\ & - [\mathcal{J}(\nu) u^\mu + \mathcal{H}^\mu(\nu)] \tilde{\mathcal{J}}(\nu') R_0^{\text{ann}}(\nu, \nu') \end{aligned} \quad (115)$$

Here, $\tilde{\mathcal{K}}^{\mu\alpha}(\nu) \equiv \mathcal{K}^{\mu\alpha}(\nu) - h^{\mu\alpha} \mathcal{J}(\nu)/3$ is the traceless part of $\mathcal{K}^{\mu\alpha}(\nu)$. Quantities with a bar such as $\tilde{\mathcal{J}}$ and $\tilde{\mathcal{H}}^\mu$ denote the radiation moments for antineutrinos. R^{in} and R^{out} are the kernels of inelastic scattering while R^{pro} and R^{ann} are the production and annihilation kernels of neutrino-pair processes. As shown in Equations (114) and (115), the radiation source term for each species and frequency involves not only the radiation at other frequency-bins but also different species (its antiparticle).

Note that the computation of neutrino opacities and the kernels are nontrivial. However, the discussion of which is beyond the scope of this work. Currently, the neutrino opacities and kernels are provided by either tabulating NuLib⁹ (O'Connor 2015) tables or coupling to our newly developed neutrino microphysics library Weakhub (H. H.-Y. Ng et al. 2024, in preparation). To maintain consistent comparisons to the work in the literature, we consider the conventional set of interactions as in Liebendörfer et al. (2005), Müller et al. (2010), O'Connor

⁹ NuLib is an open-source library, available at <http://www.nulib.org>.

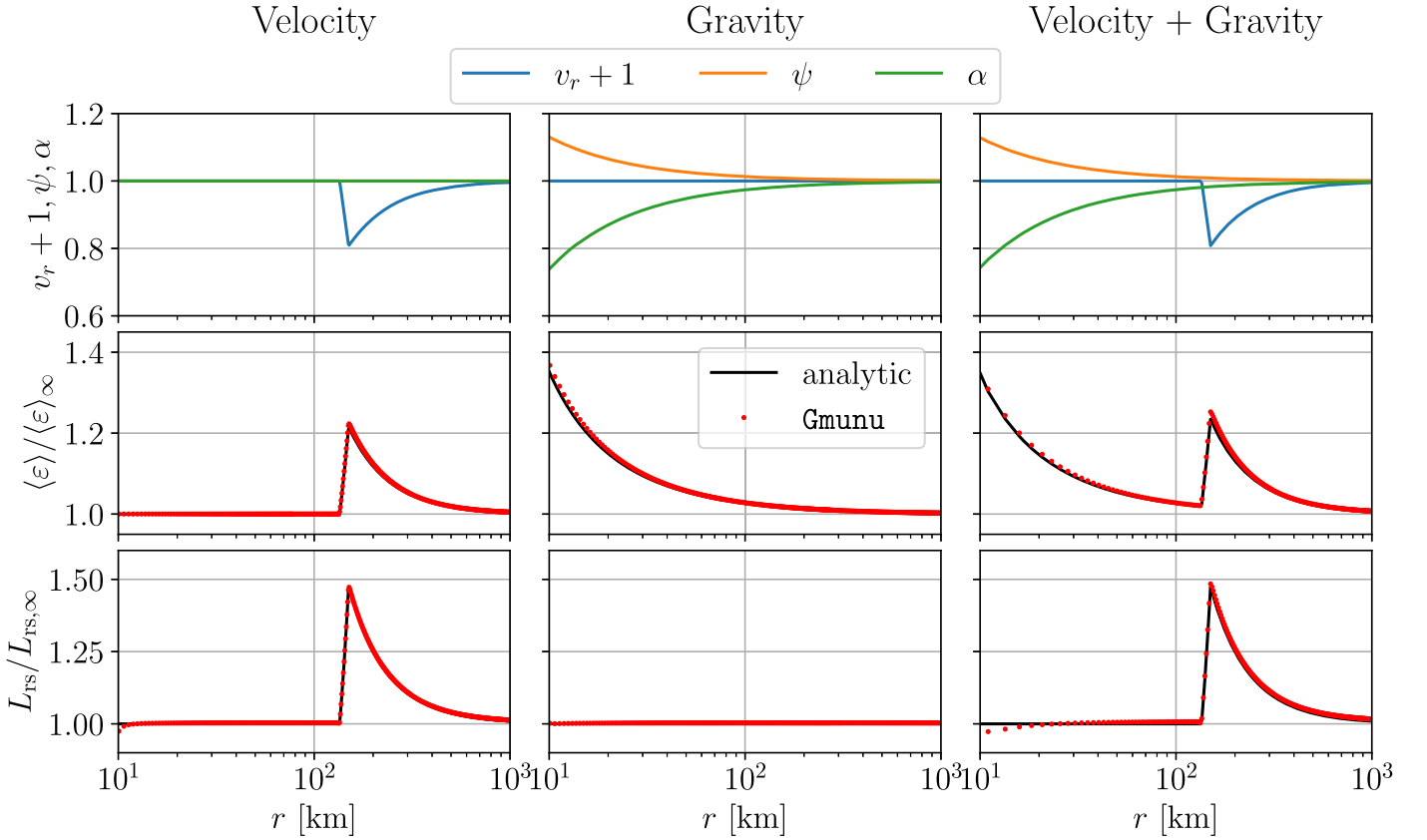


Figure 9. Comparison of the numerical solutions obtained by utilizing Gmumu (red dots) and the analytic solutions (black solid lines) of the energy advection test introduced by Müller et al. (2010). Three cases are considered in this test: namely, we consider (i) just the shape velocity profile without gravitational fields (left column); (ii) just the gravitational fields without velocity profile (middle column); and (iii) both the shape velocity profile and gravitational fields (right column). The upper panels show the shifted velocity profile $v_r + 1$ (blue solid lines), conformal factor ψ (orange solid lines), and lapse function α (green solid lines) in different cases. The middle and lower panels compare of the simulated results of the rescaled average neutrino energy $\langle \epsilon \rangle / \langle \epsilon \rangle_\infty$ and the redshift-corrected luminosity $L_{\text{rs}} / L_{\text{rs},\infty}$ obtained by utilizing Gmumu (red dots) and the analytic solutions (black solid lines). In all cases, results returned by Gmumu are in agreement with the analytic expressions. This test demonstrates that Gmumu is able to handle the frequency advection terms in the evolution of radiations, which corresponds to gravitational redshift and Doppler shift affects of the radiation with different frequencies.

(2015), and O’Connor et al. (2018) and ignoring the weak-magnetism and recoil corrections (O’Connor 2015). This set of interactions is summarized in Table 1. Note that, by following O’Connor (2015), we approximate the treatment for neutrino-pair processes such as electron–positron annihilation and nucleon–nucleon Bremsstrahlung. Specifically, the thermal processes for electron-type neutrinos and antineutrinos are not included. In addition, the full neutrino–matter interaction terms for heavy-lepton neutrinos are approximately represented with effective emissivity and absorption opacities. As a result, there is no neutrino species coupling with this set of neutrino interaction. Therefore, a multispecies multigroup implicit solver is not necessary with these neutrino interactions.

The evolution of the electron fraction Y_e , which is defined as the number of electrons per baryon, has to be included in order to describe matter in nuclear statistical equilibrium and compute the neutrino emissivity and/or opacities. Since the β -processes of ν_e and $\bar{\nu}_e$ change the electron fraction Y_e , the source term of the evolution equation of the electron fraction Y_e (see H. H.-Y. Ng et al. 2024, in preparation) is expressed as

$$s_{DY_e} = m_u \int \frac{dV_{\nu'}}{\nu'} [s_{\text{rad},\nu_e}^\mu(\nu') - s_{\text{rad},\bar{\nu}_e}^\mu(\nu')] u_\mu, \quad (116)$$

where m_u is the atomic mass unit. This coupling is treated explicitly as discussed in Section 3.6.2. Specifically, the

Table 1

Conventional Set of Neutrino Interactions Considered in This Work

Beta Processes	Neutrino-pair Processes
$\nu_e + n \leftrightarrow p + e^-$	$e^- + e^+ \leftrightarrow \nu + \bar{\nu}$
$\bar{\nu}_e + p \leftrightarrow n + e^+$	$N + N \leftrightarrow N + N + \nu + \bar{\nu}$
$\nu_e + (A, Z - 1) \leftrightarrow (A, Z) + e^-$	
Elastic scattering	Inelastic scattering
$\nu + N \leftrightarrow \nu + N$	$\nu + e^- \leftrightarrow \nu + e^-$
$\nu + (A, Z) \leftrightarrow \nu + (A, Z)$	
$\nu + \alpha \leftrightarrow \nu + \alpha$	

Note. Here we denote the electron, antielectron, and heavy-lepton neutrino as ν_e , $\bar{\nu}_e$, and ν_x , respectively. ν represents all three species of neutrino. Interactions that involve a specific type of neutrino are expressed explicitly. (A, Z) represents a heavy nucleus with a mass number of A and a proton number of Z , without including α particle. The neutrino-pair processes could be either approximately treated as effective emissivity and/or absorption opacity or handled by using the full production and/or annihilation kernels.

conserved quantity for electron fraction q_{DY_e} is updated by

$$q_{DY_e} \rightarrow q_{DY_e} + \Delta t \left\{ m_u \int \frac{dV_{\nu'}}{\nu'} [s_{\text{rad},\nu_e}^\mu(\nu') - s_{\text{rad},\bar{\nu}_e}^\mu(\nu')] u_\mu \right\} \quad (117)$$

once the radiation moments are solved implicitly.

5.2. Core Collapse of a $15 M_{\odot}$ Star in 1D

The collapse, bounce, and early post-bounce evolution of the $15 M_{\odot}$ progenitor star s15s7b2 of Woosley & Weaver (1995) has become a standard test for core-collapse supernovae simulation code (e.g., Liebendörfer et al. 2005; Müller et al. 2010; O’Connor 2015; Kuroda et al. 2016). In these works, the equation of state of Lattimer & Swesty (1991) with an incompressibility parameter of $K = 180$ MeV is used. Note that this equation of state, which has a maximum cold neutron star gravitational mass of $1.84 M_{\odot}$, has been ruled out already. For the purposes of this comparison, we use the same equation of state.

In this section, we present the core-collapse supernovae simulation with the same progenitor, and compare our result with the ones from AGILE-BOLTZTRAN, VERTEX, and GR1D (O’Connor & Ott 2010; O’Connor 2015). The data of AGILE-BOLTZTRAN and VERTEX are obtained from the online material provided in the electronic version of Liebendörfer et al. (2005) while the data of GR1D are reproduced by using the code with the settings for Section 5.1 in O’Connor (2015).¹⁰ In this subsection, we use the identical NuLib table.

5.2.1. Treatments in Different Phases

As mentioned in Section 3.6.3, avoiding full implicit treatment would significantly reduce the computational cost. In fact, in the context of core-collapse supernovae, given that the time step is properly chosen, a full implicit treatment that includes fluid variables is barely necessary even when the system is stiff (O’Connor 2015; Just et al. 2015; Mezzacappa et al. 2020). For instance, in the optically thick region, neutrinos are trapped in the fluid and are very close to weak equilibrium. The net change (absorption minus emission) of the frequency-integrated neutrinos source terms are effectively small. As a result, the change on fluid quantities due to neutrinos is negligible compared with hydrodynamical effects. In addition to the fluid quantities, depending on the stage of the collapse, it is also valid to treat part of the neutrino source terms explicitly, which could significantly reduce the size of the nonlinear system.

In practice, we split the simulation into three phases. In phase (1), the collapse begins but not extremely dynamical. We update the metric at every 0.1 ms, set the Courant–Friedrichs–Lewy (CFL) factor to be 0.8, and check the refinement criteria at every 10 iterations. In this phase, we use mode (3) (single-species single-group) radiation-interaction terms’ treatment (see Section 3.6.3). Once the maximum rest-mass density ρ is larger than $10^{12} \text{ g cm}^{-3}$, we switch to phase (2), where we update the metric at every 0.01 ms, set the CFL factor to be 0.4, and check the refinement criteria at every iteration. In this phase, we use mode (2) (single-species multi-group) radiation-interaction terms’ treatment. Core bounce is expected in this phase, which is defined as when the matter entropy per baryon is larger or equals to 3 (i.e., $s \geq 3 k_B/\text{baryon}$) in the core region. We monitor this core-bounce criteria in the core region (i.e., $r \lesssim 30$ km) at each time step in this phase. Finally, we switch to

phase (3) (post-bounce phase) 20 ms after core bounce. In this phase, the treatment for radiation-interaction terms is unchanged. We update the metric at every 0.05 ms, set the CFL factor to be 0.6, and check the refinement criteria at every 5 iterations.

Since the electron fraction Y_e is not solved consistently in the implicit step, it is possible that the change of the electron fraction is too large, resulting in a nonphysical result and eventually crashes the code. Similar to that in O’Connor (2015), Foucart et al. (2015), we monitor the change of the electron fraction Y_e at each time step. When the relative difference of the electron fraction Y_e is larger than 10^{-3} , we scale down the CFL factor by multiplying by 0.9 and continue the simulation. Otherwise, we scale up the CFL factor by dividing by 0.9 until it goes back to the corresponding setting in the particular phase of the simulation.

5.2.2. Numerical Setup

The computational domain covers $[0, 10^4]$ km for r , with the resolution $N_r = 128$, and allowing $l_{\text{max}} = 12$ mesh levels. For the refinement criteria, we apply the Löhner’s error estimator (Löhner 1987; Cheong et al. 2021) on the logarithmic rest-mass density $\log_{10}(\rho)$. This can effectively capture the sudden change of rest-mass density (usually arise at shock) while keeping the refinement low elsewhere. On top of the error estimator, to better resolve the high density region of the star, we require the block to the finest level l_{max} when any of the rest-mass density ρ in this block is larger than $\rho_{\text{thr}} \equiv 5 \times 10^{12} \text{ g cm}^{-3}$. Since we are mainly interested in the inner part of the massive star in this work, we further impose a maximum allowed refinement level at a different location. For instance, when the smallest radius r_{min} in a block is smaller than 100 km (i.e., when $r_{\text{min}} \leq 100$ km), the highest allowed refinement level is l_{max} . Also, when $r_{\text{min}} \leq 2 \times 100$ km, the highest allowed refinement level is $l_{\text{max}} - 1$, and so on and so forth. We also enforce the refinement level to be lowest when the block contains outer boundaries.

The frequency-space is discretized into 18 groups logarithmically from 1 to $280 \text{ MeV } h^{-1}$. We evolve three species of neutrinos, namely, the electron neutrino ν_e , antielectron neutrino $\bar{\nu}_e$ and heavy-lepton neutrino ν_x , where the muon and tauon neutrinos (i.e., ν_{μ} , $\bar{\nu}_{\mu}$, ν_{τ} and $\bar{\nu}_{\tau}$) are grouped into ν_x .

5.2.3. Results

Figure 10 shows the evolution of central matter entropy per baryon s , central electron fraction Y_e , and lepton number fraction $Y_{\text{lep}} \equiv Y_e + Y_{\nu}$ as functions of central density ρ_c of the collapsing $15 M_{\odot}$ star before core-bounce. During the deleptonization phase, the entropy per baryon increases due to neutrino interaction. The core deleptonization ends when the central density reaches approximately $2 \times 10^{12} \text{ g cm}^{-3}$. Since then, the neutrinos are mostly trapped, where the lepton number fraction remains almost unchanged. In this stage, the inner core collapses adiabatically, and the entropy per baryon remains nearly constant. It is worthwhile to point out that the evolution of lepton numbers is highly sensitive to the implementations of the multigroup coupling, radiation space advection in optically thick regions, and advection in frequency-space for lepton number conservation, even when the exact same neutrino microphysics is used (O’Connor 2015; Kuroda et al. 2016).

¹⁰ GR1D is an open-source neutrino radiation transport code for core-collapse supernovae (O’Connor & Ott 2010; O’Connor 2015). The GR1D code, and also the parameter files, equation of state, and the NuLib tables used in O’Connor (2015) are available at <http://www.GR1Dcode.org>. Note that, since the conformally flat metric equations are equivalent to the Einstein equations in spherical symmetry, our results here are fully general-relativistic as in GR1D and AGILE-BOLTZTRAN.

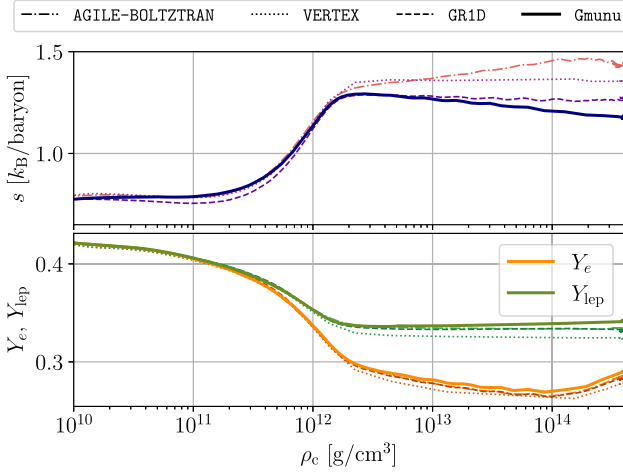


Figure 10. Evolution of central matter entropy per baryon (s , upper panel), electron, and total lepton number fractions (Y_e and $Y_{\text{lep}} \equiv Y_e + Y_\nu$, lower panel) as functions of central density ρ_c of a collapsing $15 M_\odot$ star before core-bounce. The solid lines show the numerical results obtained by Gmunu. Note that the evolution of lepton numbers is highly sensitive to the implementations of the multigroup coupling and radiation advection in optically thick regions. Our results agree very well with the results of AGILE-BOLTZTRAN (dashed-dotted lines), VERTEX (dotted lines), and GR1D (dashed lines).

Strong repulsive forces of nuclear matter arise when the rest-mass density exceeds the nuclear saturation densities. This results in core bounce, and forms the bounce shock. In our simulation, the core bounces at $t_{\text{bounce}} \approx 178.21$ ms. In Figure 11, we compare the radial profiles of several quantities among different codes at the moment of core bounce. In particular, we compare rest-mass density ρ , radial velocity v^r/c , matter temperature T , matter entropy per baryon s , neutrino root mean squared energy $\sqrt{\langle \epsilon_\nu^2 \rangle}$, and electron fraction Y_e . Here, the neutrino root mean squared energy is defined by

$$\sqrt{\langle \epsilon^2 \rangle} \equiv \frac{\int_0^\infty \nu J dV_\nu}{\int_0^\infty J / \nu dV_\nu}. \quad (118)$$

As shown in the figure, a shock is formed at ~ 10 km, and the matter entropy reaches $3 k_B/\text{baryon}$ at the shock. Since the gauge adopted in Gmunu is different from the one in AGILE-BOLTZTRAN, VERTEX, and GR1D, a transformation is needed in order to compare the results directly. The areal circumferential radius r_{circ} used in Liebendörfer et al. (2005) can be expressed in terms of the isotropic radial coordinate r_{iso} and the conformal factor ψ by Marek et al. (2006), Müller et al. (2010):

$$r_{\text{circ}} = \psi^2 r_{\text{iso}}. \quad (119)$$

Below, we simply use r to denote the areal circumferential radius r_{circ} .

Although the results produced by utilizing Gmunu are quantitatively in good agreement with the reference models by using AGILE-BOLTZTRAN, VERTEX, and GR1D, there are some deviations in the inner part of the star. In particular, the hydrodynamical quantities such as entropy s , electron fraction Y_e , and temperature T are slightly deviated from the reference solutions when the central rest-mass density ρ_c goes beyond $\sim 2 \times 10^{12} \text{ g cm}^{-3}$ (see Figure 10) and for the region where $r \lesssim 10$ km (see Figure 11). These deviations could be due to the

following three reasons. First, different implementations of nuclear equation of state (see also the discussion in O’Connor 2015) and the primitive recovery are very likely to cause the differences of the entropy and so as other hydrodynamical quantities. Second, although both our code and GR1D couple the hydrodynamical quantities directly in the implicit radiation moment solver, such a coupling will be applied twice for each time step when IMEX-SSP2(2,2,2) is used. The discrepancy caused by the direct coupling might be accumulated faster than in the first-order IMEX method. Solving the entire evolution system including the hydrodynamical quantities implicitly will lead to more accurate and consistent results, which is left as future work. Third, since adaptive mesh refinement is used in our simulations, the resolution at the center part is not fixed during the simulation, and depends on the rest-mass density ρ , which changes rapidly right before the core bounce. The numerical errors due to such rapid refinements are some of the sources of the error. Refinement strategies that have better balance between the accuracy and computational cost will be explored in the future.

The far-field neutrino root mean squared energies and luminosities are important to the predictions of observation, which are highly sensitive to the microphysics considered and the implementation. Therefore, it is necessary to show and compare these key neutrino quantities among the codes. In Figure 12, we show the time evolution of far-field neutrino root mean squared energies $\sqrt{\langle \epsilon_\nu^2 \rangle}$ and luminosities L_ν , measured by an observer comoving with fluid at 500 km. As shown in the figure, the agreement between Gmunu, AGILE-BOLTZTRAN, and GR1D is exceptional. This is expected since both of the two simulations adopt two-moment schemes and use identical neutrino opacities and kernels table.

The shock radius evolution is also important in the core-collapse supernovae context. Figure 13 shows the time evolution of the shock radius. Our results agree very well with GR1D for $t - t_{\text{bounce}} \lesssim 40$ ms. After that, the shock radius predicted by Gmunu is roughly 10 km larger than GR1D’s, which lies between AGILE-BOLTZTRAN and GR1D.

The results presented above, especially the neutrino signals, are relatively closer to GR1D’s among the codes we have compared. Despite the neutrino interactions considered being mostly the same in these runs, the way of how the neutrino opacities and kernels are computed could be different (e.g., the resolutions in energy space, number of species evolved are different). Moreover, as mentioned above, approximated treatments for neutrino-pair processes are adopted in the NuLib table in this test. Due to the fact that the same NuLib table with the same resolution in energy (frequency) space is used in both GR1D and Gmunu, the corresponding results are expected to be very similar.

5.3. Hot Neutron Star

For the second application example, we study the radial oscillation and neutrino emissions of a hot neutron star by following Galeazzi et al. (2013), Neilsen et al. (2014). In particular, we consider a nonrotating equilibrium model with the Shen–Horowitz–Teige equation of state from Shen et al. (2011) with central rest-mass density $\rho_c = 9.3 \times 10^{14} \text{ g cm}^{-3}$. The star has a constant entropy per baryon $s = 1 k_B/\text{baryon}$ and in β equilibrium. The temperature of which is roughly 30 MeV at the center of the star. The gravitational mass and the circumferential radius of this neutron star are $M_{\text{grav}} = 2.741 M_\odot$,

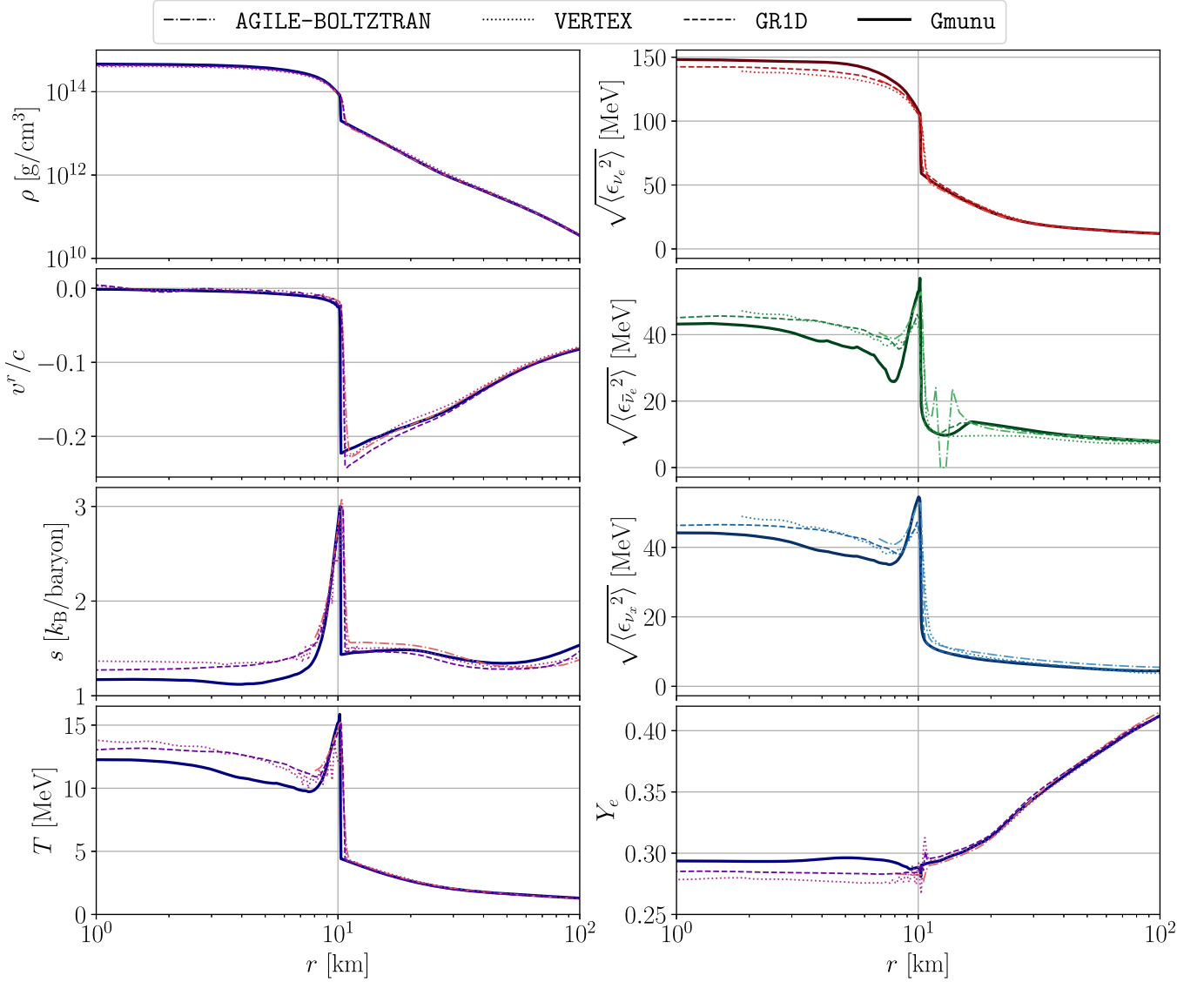


Figure 11. Comparison of the radial profiles of several quantities between our code Gmunu and the reference codes (AGILE-BOLTZTRAN, VERTEX, and GR1D) at the moment of core bounce. For instance, we compare rest-mass density ρ , radial velocity v^r/c , matter temperature T , matter entropy per baryon s , neutrino root mean squared energy $\sqrt{\langle \epsilon_{\nu_i}^2 \rangle}$, and electron fraction Y_e . The solid lines show the numerical results obtained by Gmunu. A shock is formed at ~ 10 km, and the matter entropy reaches $3 k_B/\text{baryon}$ at the shock. Our results generated by Gmunu are quantitatively agreeing with the reference solution produced by AGILE-BOLTZTRAN (dashed-dotted lines), VERTEX (dotted lines), and GR1D (dashed lines).

and $R_{\text{circ}} = 14$ km, respectively. As discussed in Galeazzi et al. (2013), this neutron star is mostly opaque to neutrinos, and the neutrino diffusion timescale ($\mathcal{O}(\text{s})$) is much longer than its dynamical timescale ($\mathcal{O}(\text{ms})$). The neutron star is expected to be cooling slowly. In addition, since the emitted neutrino will mostly be reabsorbed in the hot and dense region, the neutrino emission from the system mostly comes from the outer layer of the neutron star. Therefore, this test problem, especially the neutrino emissions, is highly sensitive to the low density and/or atmosphere treatment.

The initial neutron star models are generated with the modified version of the open-source code XNS¹¹ (Bucciantini & Del Zanna 2011; Pili et al. 2014, 2015, 2017). We simulate this initial model in 1D spherical coordinates, where the computational domain covers $0 \leq r \leq 400$ (≈ 591 km), with the resolution $N_r = 256$ and allowing 4 refinement levels (i.e., an

effective resolution of $N_r = 2048$). For the simulations of neutron stars, we used the same refinement setting as in our previous work (Cheong et al. 2021). In particular, we defined a relativistic gravitational potential $\Phi \equiv 1 - \alpha$. For any Φ larger than the maximum potential Φ_{max} (which is set as 0.2 in this work), the block is set to be the finest. While for the second-finest level, the same check is performed with a new maximum potential, which is half of the previous one, and so on and so forth. The grid is fixed after the initialization. In this test, the second-order monotized central limiter (van Leer 1974) is used. The rest-mass density of the atmosphere ρ_{atmo} is set to be 10^3 g cm^{-3} . The spacetime is kept fixed during the entire simulation (i.e., we evolve this system with Cowling approximation).

While different neutrino microphysics inputs are expected to affect the neutrino signals, the neutrino interactions we can include are so far limited by NuLib. Instead of considering the same set of neutrino interactions as in Galeazzi et al. (2013),

¹¹ Available at <https://www.arcetri.inaf.it/science/ahead/XNS/index.html>.

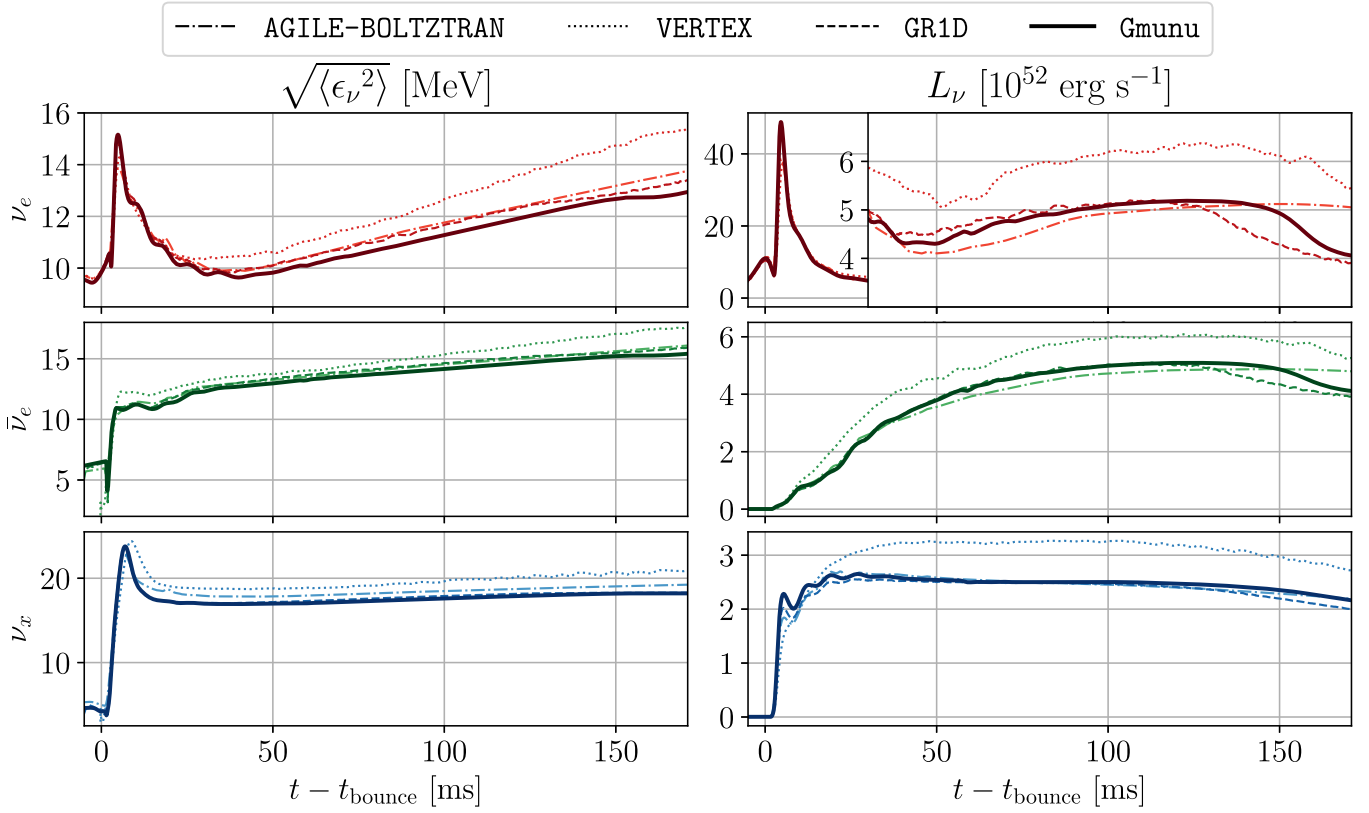


Figure 12. Time evolution of far-field neutrino root mean squared energies ($\sqrt{\langle \epsilon_\nu^2 \rangle}$, left panel) and luminosities (L_ν , right panel) measured by an observer comoving with fluid at 500 km of a collapsing $15 M_\odot$ star. The solid lines show the numerical results obtained by Gmnu. To compare the deleptonization burst and the early post-bounce evolution of the luminosity of electron-type neutrino more in detail, we changed the scale after $t > 30$ ms (upper right panel). The evolution of these neutrino quantities is again highly sensitive to the implementation and essential to the predictions of observational signatures. Our results agree very well with the reference results produced by AGILE-BOLTZTRAN (dashed-dotted lines), VERTEX (dotted lines), and GR1D (dashed lines).

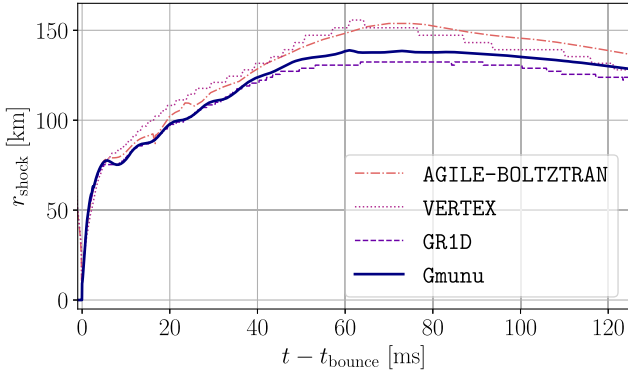


Figure 13. Time evolution of the shock radius. The solid lines show the numerical results obtained by Gmnu. The reference results produced by AGILE-BOLTZTRAN, VERTEX, and GR1D are shown with dashed-dotted line, dotted line, and dashed line, respectively. The shock radius predicted by Gmnu is mostly agreeing with GR1D for $t - t_{\text{bounce}} \lesssim 40$ ms while it is approximately 10 km larger since then. Since then, it goes between the result of AGILE-BOLTZTRAN and GR1D.

Neilsen et al. (2014), we adopt essentially the same set of interactions as described in Section 5.1, except that the thermal processes for electron-type neutrinos and antineutrinos (i.e., $e^- + e^+ \rightarrow \nu_e + \bar{\nu}_e$) are also included. The inclusion of this interaction is to additionally test our *multispecies multigroup* implicit solver, since the coupling of electron-type neutrinos ν_e and antineutrinos $\bar{\nu}_e$ has to be taken into account. Although this test problem is expected to be sensitive to the low density and/or atmosphere treatment, to achieve a stable evolution, the

neutrino opacities and kernels are used only when the rest-mass density ρ is larger than $10^{11} \text{ g cm}^{-3}$, which is 8 orders of magnitude larger than the atmosphere density ρ_{atmo} . The neutrino moments are initialized by evolving the radiation sector while keeping the hydrodynamical profile fixed until the system reaches equilibrium. In this test, we evolve the neutrinos while keeping the hydrodynamical profile fixed for 5 ms before the dynamical simulation.

The neutron star relaxes to its new equilibrium configurations during the first few milliseconds in our simulation, where the surface of the star is neutron-rich ($Y_e \sim 0.1$) with high temperature ($T \sim 10 \text{ MeV}$), which is similar to the case reported in Neilsen et al. (2014). The upper panel of Figure 14 shows the relative variation of the central rest-mass density ρ_c in time while the middle panel shows the time evolution of far-field neutrino luminosities L_ν measured by an observer with fluid at 100 km. Since the neutrino signals take around 3 ms to reach the extraction point, the luminosities of all neutrinos are zeros before 3 ms. The luminosities we obtained at the stationary state are at the order of $10^{51} \text{ erg s}^{-1}$, which are slightly larger than the one reported in Neilsen et al. (2014) (of the order of $10^{50-51} \text{ erg s}^{-1}$) while much lower than the one reported in Galeazzi et al. (2013) (of the order of $10^{52-53} \text{ erg s}^{-1}$). In addition, the luminosity of heavy-lepton neutrino L_{ν_x} is found to be highly oscillating. This is mainly because the opacities and kernels for low density region ($\rho \leq 10^{11} \text{ g cm}^{-3}$) are ignored while the interactions of heavy-lepton neutron are sensitive in this region.

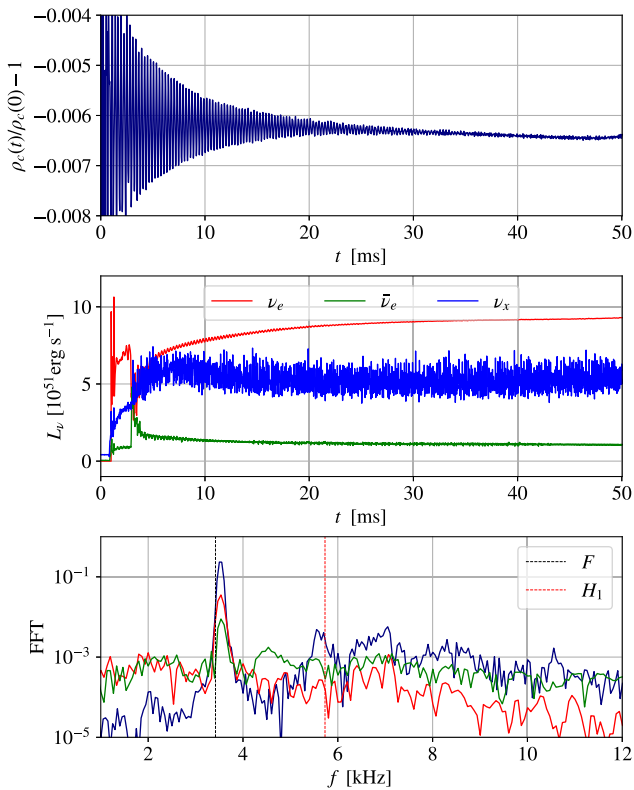


Figure 14. Upper panel: the relative variation of the central rest-mass density ρ_c of the hot neutron star in time. Middle panel: time evolution of far-field neutrino luminosities measured by an observer comoving with fluid at 100 km of a hot neutron star. The luminosities are zero for $t \lesssim 3$ ms as the neutrino signals are not yet arrived at the extraction point. Lower panel: the fast Fourier transform of the central rest-mass density, and the luminosities of electron and antielectron neutrinos. The amplitude of the fast Fourier transform of the central rest-mass density (navy solid line) has been rescaled for a better visualization. The vertical dashed lines represent the known eigenmode frequencies (Galeazzi et al. 2013). The eigenmode frequencies we obtained are in good agreement with the one in Galeazzi et al. (2013), Neilsen et al. (2014).

The lower panel of Figure 14 shows the fast Fourier transform of the central rest-mass density, and the luminosities of electron and antielectron neutrinos with the time window $t \in [5, 20]$ ms. The fast Fourier transform of the luminosity of heavy-lepton neutrino is not included due to its highly oscillatory nature, and the frequency does not correspond to any of the known normal mode oscillations of the neutron star. To better visualize the result, the amplitude of the fast Fourier transform of the central rest-mass density has been rescaled by a factor of 1000. The eigenmode frequencies obtained from our simulations agree with the one in Galeazzi et al. (2013), Neilsen et al. (2014).

Despite the same model, the neutrino luminosities are expected to be different from those in Galeazzi et al. (2013), Neilsen et al. (2014) for two reasons: (i) the neutrino luminosities are highly sensitive to the neutrino and/or atmosphere treatment adopted in the simulation code (Neilsen et al. 2014), and (ii) the neutrino interactions considered here are not identical to the one in Galeazzi et al. (2013), Neilsen et al. (2014), which could significantly alter the outcome of the neutrino signals. The test here is to qualitatively compare the results reported in the literature, detailed investigations on a better low density treatment; and how the neutrino treatment affects the hot neutron star modeling will be left as future work.

6. Conclusions

We present the new implementation of the two-moment-based multifrequency multispecies general-relativistic radiation hydrodynamics module in our code `Gmunu`.

Our implementation has been tested with several benchmarking tests, which range from special-relativistic to general-relativistic, from optically thick to optically thin, and from frequency-integrated to frequency-dependent cases. These test results demonstrate that our code `Gmunu` is able to capture the evolution of radiation fields even in the mildly relativistic cases in either optically thin or thick regime.

In addition, we demonstrate that our implicit solvers can robustly solve the largely coupled system, where all the neutrino species at different frequency-bins are coupled altogether, by performing simulations of a collapsing massive star and a hot neutron star. In the core-collapse supernova test, we present the pre-bounce, core-bounce, and early post-bounce evolution of a $15 M_\odot$ progenitor star. Also, we show the simulated fair-field neutrino root mean squared energies and luminosities, which are essential to observational astrophysics. Despite these neutrino quantities that are highly sensitive to the implementation of the radiation transport and implicit treatment for neutrino–matter interaction, `Gmunu` produces a consistent result, which agrees with other neutrino transport codes. On the other hand, in the hot neutron star test, our normal mode frequencies are in agreement with the one reported in the literature. Moreover, the order of magnitude of the neutrino luminosities extracted from our simulation lie between the one presented in Galeazzi et al. (2013), Neilsen et al. (2014) for the same model. Despite the neutrino treatment and interaction considered being different, our results qualitatively agree with those from the literature.

Although our current implementation works properly for the test problems presented, further investigations are needed to improve the module. In particular, the fluid acceleration terms are not properly included in this work. Including these terms and assessing their impacts on mildly and/or highly relativistic terms are essential to neutron star merger simulations. Besides, solving the entire evolution system including the fluid quantities consistently would lead to more stable and accurate simulations. Implementing more-advanced full implicit treatments that allow us to fully solve the system with reasonable computational cost (e.g., Skinner et al. 2019; Laiu et al. 2021) is also important for astrophysical applications. These aspects will be investigated in future work.

Acknowledgments

We wish to thank Francois Foucart for the helpful discussions on implementations and tests, and detailed comments on the manuscript. We also wish to thank David Radice for the helpful discussions on the treatment of frequency-space advection and initial guess of the implicit step, and Tia Martineau for the detailed proofreading and suggestions on the manuscript. P.C.K.C. acknowledges support from NSF grant PHY-2020275 (Network for Neutrinos, Nuclear Astrophysics, and Symmetries (N3AS)). H.H.Y.N. is supported by the ERC Advanced Grant “JETSET: Launching, propagation and emission of relativistic jets from binary mergers and across mass scales” (grant No. 884631). The simulations in this work have been performed on the third University of New Hampshire supercomputer Marvin, also

known as Plasma, which is supported by NSF/Major Research Instrumentation program under grant No. AGS-1919310. This work was partially supported by grants from the Research Grants Council of the Hong Kong (project No. CUHK14306419), from the Croucher Innovation Award from the Croucher Foundation Hong Kong, and from the Direct Grant for Research from the Research Committee of the Chinese University of Hong Kong.

Software. The results of this work were produced by utilizing Gmnu (Cheong et al. 2020, 2021, 2022; H. H.-Y. Ng et al. 2024, in preparation), where the tabulated neutrino interaction was provided with Nulib (O'Connor 2015). GR1D (O'Connor & Ott 2010; O'Connor 2015) was also used to generate one of the reference solutions. We also modified XNS (Bucciantini & Del Zanna 2011; Pili et al. 2014, 2015, 2017) to generate the initial data of a hot neutron star. The data of the simulations were post-processed and visualized with yt (Turk et al. 2011), NumPy (Harris et al. 2020), pandas (McKinney 2010; pandas development team 2020), SciPy (Virtanen et al. 2020), and Matplotlib (Hunter 2007; Caswell et al. 2023).

Appendix A Jacobian of the Monochromatic Source Terms

Note that the emission and/or absorption and elastic scattering source terms $S_{E/A}^\mu$ and S_{ES}^μ are monochromatic, i.e., at a given radiation frequency ν , the calculation of the radiation emissivity, absorption, and scattering coefficients $\eta(\nu)$, $\kappa_a(\nu)$, and $\kappa_s(\nu)$ does not depend on other radiation frequencies $\nu' \neq \nu$, as shown in Equations (8) and (9). The interaction source terms can be largely simplified when only these two source terms are considered. In this case, the radiation four-force S_{rad}^μ can be reduced to

$$S_{\text{rad}}^\mu = S_{E/A}^\mu + S_{ES}^\mu \\ = (\eta - \kappa_a \mathcal{J}) u^\mu - (\kappa_a + \kappa_s) \mathcal{H}^\mu. \quad (\text{A1})$$

The corresponding 3+1 radiation–fluid interaction source terms for s_{rad} now become

$$s_{\text{rad}\mathcal{E}} = \alpha \psi^6 \sqrt{\hat{\gamma}/\hat{\gamma}} W \{ \eta + \kappa_s \mathcal{J} - \kappa_{as} (\mathcal{E} - \mathcal{F}_i v^i) \}; \quad (\text{A2})$$

$$s_{\text{rad}\mathcal{F}_i} = \alpha \psi^6 \sqrt{\hat{\gamma}/\hat{\gamma}} \{ (\eta - \kappa_a \mathcal{J}) W v_i - \kappa_{as} \mathcal{H}_i \}; \quad (\text{A3})$$

where $\kappa_{as} \equiv \kappa_a + \kappa_s$ is the opacity (absorption plus scattering coefficients). These are the source terms adopted in most of the gray moment codes (e.g., Radice et al. 2022). The corresponding Jacobian $\partial[s_{\text{rad}}]_i/\partial q_j$, which is needed to calculate the Jacobian in the implicit step discussed in Section 3.6, can be evaluated analytically as in Radice et al. (2022). For completeness, we include the detailed expression of $\partial[s_{\text{stiff}}]_i/\partial q_j$, where

$$s_{\text{stiff}} \equiv \frac{s_{\text{rad}}}{\psi^6 \sqrt{\hat{\gamma}/\hat{\gamma}}} \quad (\text{A4})$$

is the undentised source terms. Below, we denote

$$\hat{J}_{ab} \equiv \frac{\partial[s_{\text{stiff}}]_a}{\partial q_b}; \quad (\text{A5})$$

where $a, b = 0, 1, 2, 3$. Specifically, the equations for \hat{J}_{ab} are

$$\hat{J}_{00} = -W \left(\kappa_{as} - \kappa_s \frac{\partial \mathcal{J}}{\partial \mathcal{E}} \right); \quad (\text{A6})$$

$$\hat{J}_{0j} = W \left(\kappa_{as} v^j + \kappa_s \frac{\partial \mathcal{J}}{\partial \mathcal{F}_j} \right); \quad (\text{A7})$$

$$\hat{J}_{i0} = - \left(\kappa_{as} \frac{\partial \mathcal{H}_i}{\partial \mathcal{E}} + W \kappa_a \frac{\partial \mathcal{J}}{\partial \mathcal{E}} v_i \right); \quad (\text{A8})$$

$$\hat{J}_{ij} = - \left(\kappa_{as} \frac{\partial \mathcal{H}_i}{\partial \mathcal{F}_j} + W \kappa_a \frac{\partial \mathcal{J}}{\partial \mathcal{F}_j} v_i \right). \quad (\text{A9})$$

The corresponding derivatives are

$$\frac{\partial \mathcal{J}}{\partial \mathcal{E}} = W^2 + d_{\text{thin}} (v \cdot \hat{f})^2 W^2 \\ + d_{\text{thick}} \frac{(3 - 2W^2)(W^2 - 1)}{1 + 2W^2}, \quad (\text{A10})$$

$$\frac{\partial \mathcal{J}}{\partial \mathcal{F}_j} = \mathcal{J}_{\mathcal{F}}^v v^j + \mathcal{J}_{\mathcal{F}}^f \hat{f}^j, \quad (\text{A11})$$

$$\frac{\partial \mathcal{H}_i}{\partial \mathcal{E}} = \mathcal{H}_{\mathcal{E}}^v v_i + \mathcal{H}_{\mathcal{E}}^f \hat{f}_i, \quad (\text{A12})$$

$$\frac{\partial \mathcal{H}_i}{\partial \mathcal{F}_j} = \mathcal{H}_{\mathcal{F}}^\delta \delta_i^j + \mathcal{H}_{\mathcal{F}}^{vv} v_i v^j + \mathcal{H}_{\mathcal{F}}^{ff} \hat{f}_i \hat{f}_j \\ + \mathcal{H}_{\mathcal{F}}^{vf} v_i \hat{f}_j + \mathcal{H}_{\mathcal{F}}^{fv} \hat{f}_i v_j, \quad (\text{A13})$$

where we have defined $\hat{f}_i \equiv \mathcal{F}_i/\sqrt{\mathcal{F}^2}$, and

$$\mathcal{J}_{\mathcal{F}}^v = 2W^2 \left[-1 + d_{\text{thin}} \mathcal{E} \frac{v \cdot \hat{f}}{\mathcal{F}} + d_{\text{thick}} \frac{W^2 - 1}{1 + 2W^2} \right], \quad (\text{A14})$$

$$\mathcal{J}_{\mathcal{F}}^f = -2d_{\text{thin}} W^2 \mathcal{E} \frac{(v \cdot \hat{f})^2}{\mathcal{F}}, \quad (\text{A15})$$

$$\mathcal{H}_{\mathcal{E}}^v = W^3 \left[-1 - d_{\text{thin}} (v \cdot \hat{f})^2 + d_{\text{thick}} \frac{2W^2 - 3}{1 + 2W^2} \right], \quad (\text{A16})$$

$$\mathcal{H}_{\mathcal{E}}^f = -d_{\text{thin}} W (v \cdot \hat{f}) \quad (\text{A17})$$

$$\mathcal{H}_{\mathcal{F}}^\delta = W \left[1 - d_{\text{thin}} \mathcal{E} \frac{(v \cdot \hat{f})}{\mathcal{F}} - d_{\text{thick}} v^2 \right], \quad (\text{A18})$$

$$\mathcal{H}_{\mathcal{F}}^{vv} = 2W^3 \left[1 - d_{\text{thin}} \mathcal{E} \frac{(v \cdot \hat{f})}{\mathcal{F}} \right. \\ \left. - d_{\text{thick}} \left(1 - \frac{4W^2 + 1}{2W^2(2W^2 + 1)} \right) \right], \quad (\text{A19})$$

$$\mathcal{H}_{\mathcal{F}}^{ff} = 2d_{\text{thin}} W \mathcal{E} \frac{(v \cdot \hat{f})}{\mathcal{F}}, \quad (\text{A20})$$

$$\mathcal{H}_{\mathcal{F}}^{vf} = -W \mathcal{J}_{\mathcal{F}}^f, \quad (\text{A21})$$

and

$$\mathcal{H}_{\mathcal{F}}^{fv} = -d_{\text{thin}} W \frac{\mathcal{E}}{\mathcal{F}}. \quad (\text{A22})$$

Moreover, the source terms in the evolution equation of electron fraction Y_e are also simplified in this case. In particular, the contraction of the interaction source and four-velocity term $s_{\text{rad}}^\mu u_\mu$ in the right-hand side of Equation (116) can now be

written as follows:

$$s_{\text{rad}}^{\mu} u_{\mu} = \eta - \kappa_a \mathcal{J}. \quad (\text{A23})$$

Appendix B

Decomposition of Fluid-frame Moments

Although the fluid-frame moments $\{\mathcal{J}, \mathcal{H}^{\mu}\}$ can be computed by contracting the energy-momentum tensor $\mathcal{T}^{\mu\nu}$ with the comoving velocities u^{μ} , it is useful to work out the contraction further, and directly express the fluid-frame moments $\{\mathcal{J}, \mathcal{H}^{\mu}\}$ in terms of observer-frame moments $\{\mathcal{E}, \mathcal{F}^i\}$. As in Deppe et al. (2022), Radice et al. (2022), we decompose $\{\mathcal{J}, \mathcal{H}^{\mu}, \mathcal{H}^{\mu}\mathcal{H}_{\mu}\}$ as

$$\mathcal{J} = J_{(1)} + d_{\text{thin}} J_{(2)} + d_{\text{thick}} J_{(3)}, \quad (\text{B1})$$

$$\begin{aligned} \mathcal{H}_{\mu} &= -(H_{(1)} + d_{\text{thin}} H_{(2)} + d_{\text{thick}} H_{(3)}) n_{\mu} \\ &- (H_{(4)} + d_{\text{thin}} H_{(5)} + d_{\text{thick}} H_{(6)}) v_{\mu} \\ &- (H_{(7)} + d_{\text{thin}} H_{(8)} + d_{\text{thick}} H_{(9)}) \mathcal{F}_{\mu}, \end{aligned} \quad (\text{B2})$$

$$\begin{aligned} \mathcal{H}^2 &= [H^2]_{(1)} + d_{\text{thin}} [H^2]_{(2)} + d_{\text{thick}} [H^2]_{(3)} \\ &+ d_{\text{thin}}^2 [H^2]_{(4)} + d_{\text{thick}}^2 [H^2]_{(5)} + d_{\text{thin}} d_{\text{thick}} [H^2]_{(6)}, \end{aligned} \quad (\text{B3})$$

where

$$J_{(1)} = W^2 (\mathcal{E} - 2v^i \mathcal{F}_i), \quad (\text{B4})$$

$$J_{(2)} = W^2 \mathcal{E} \frac{(v^i \mathcal{F}_i)^2}{\mathcal{F}^i \mathcal{F}_i}, \quad (\text{B5})$$

$$J_{(3)} = \frac{W^2 - 1}{2W^2 + 1} [(3 - 2W^2) \mathcal{E} + 4W^2 v^i \mathcal{F}_i], \quad (\text{B6})$$

$$H_{(1)} = W (J_{(1)} + v^i \mathcal{F}_i - \mathcal{E}), \quad (\text{B7})$$

$$H_{(2)} = W J_{(2)}, \quad (\text{B8})$$

$$H_{(3)} = W J_{(3)}, \quad (\text{B9})$$

$$H_{(4)} = W J_{(1)}, \quad (\text{B10})$$

$$H_{(5)} = H_{(2)}, \quad (\text{B11})$$

$$H_{(6)} = H_{(3)} + \frac{W}{2W^2 + 1} [(3 - 2W^2) \mathcal{E} - (1 - 2W^2) v^i \mathcal{F}_i], \quad (\text{B12})$$

$$H_{(7)} = -W, \quad (\text{B13})$$

$$H_{(8)} = W \mathcal{E} \frac{(v^i \mathcal{F}_i)}{\mathcal{F}^i \mathcal{F}_i}, \quad (\text{B14})$$

$$H_{(9)} = W v^i v_i, \quad (\text{B15})$$

$$\begin{aligned} [H^2]_{(1)} &= -H_{(1)}^2 + H_{(4)}^2 v^2 + H_{(7)}^2 \mathcal{F}^2 \\ &+ 2H_{(4)} H_{(7)} v^i \mathcal{F}_i, \end{aligned} \quad (\text{B16})$$

$$\begin{aligned} [H^2]_{(2)} &= 2(H_{(4)} H_{(5)} v^2 + H_{(7)} H_{(8)} \mathcal{F}^2 \\ &+ H_{(4)} H_{(8)} v^i \mathcal{F}_i + H_{(7)} H_{(5)} v^i \mathcal{F}_i - H_{(1)} H_{(2)}), \end{aligned} \quad (\text{B17})$$

$$\begin{aligned} [H^2]_{(3)} &= 2(H_{(4)} H_{(6)} v^2 + H_{(7)} H_{(9)} \mathcal{F}^2 \\ &+ H_{(4)} H_{(9)} v^i \mathcal{F}_i + H_{(7)} H_{(6)} v^i \mathcal{F}_i - H_{(1)} H_{(3)}), \end{aligned} \quad (\text{B18})$$



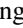
$$\begin{aligned} [H^2]_{(4)} &= 2(H_{(5)} H_{(6)} v^2 + H_{(8)} H_{(9)} \mathcal{F}^2 \\ &+ H_{(5)} H_{(9)} v^i \mathcal{F}_i + H_{(8)} H_{(6)} v^i \mathcal{F}_i - H_{(2)} H_{(3)}), \end{aligned} \quad (\text{B19})$$

$$\begin{aligned} [H^2]_{(5)} &= -H_{(3)}^2 + H_{(6)}^2 v^2 + H_{(9)}^2 \mathcal{F}^2 \\ &+ 2H_{(6)} H_{(9)} v^i \mathcal{F}_i, \end{aligned} \quad (\text{B20})$$

and

$$\begin{aligned} [H^2]_{(6)} &= -H_{(2)}^2 + H_{(5)}^2 v^2 + H_{(8)}^2 \mathcal{F}^2 \\ &+ 2H_{(5)} H_{(8)} v^i \mathcal{F}_i. \end{aligned} \quad (\text{B21})$$

ORCID iDs

Patrick Chi-Kit Cheong (張志杰)  <https://orcid.org/0000-0003-1449-3363>
 Harry Ho-Yin Ng  <https://orcid.org/0000-0003-3453-7394>
 Alan Tsz-Lok Lam  <https://orcid.org/0000-0002-1307-1401>
 Tjonnie Guang Feng Li  <https://orcid.org/0000-0003-4297-7365>

References

- Abdikamalov, E., Burrows, A., Ott, C. D., et al. 2012, *ApJ*, **755**, 111
 Anninos, P., & Fragile, P. C. 2020, *ApJ*, **900**, 71
 Ascher, U. M., Ruuth, S. J., & Spiteri, R. J. 1997, *ApNM*, **25**, 151
 Audit, E., Charrier, P., Chièze, J. P., & Dubroca, B. 2002, arXiv:astro-ph/0206281
 Baumgarte, T. W., & Shapiro, S. L. 2020, *PhRvD*, **102**, 104001
 Bollig, R., Yadav, N., Kresse, D., et al. 2021, *ApJ*, **915**, 28
 Bucciantini, N., & Del Zanna, L. 2011, *A&A*, **528**, A101
 Buchler, J. R. 1979, *JQSRT*, **22**, 293
 Burrows, A. 2013, *RvMP*, **85**, 245
 Burrows, A., Radice, D., Vartanyan, D., et al. 2020, *MNRAS*, **491**, 2715
 Burrows, A., & Vartanyan, D. 2021, *Natur*, **589**, 29
 Cardall, C. Y., Endeve, E., & Mezzacappa, A. 2013, *PhRvD*, **87**, 103004
 Caswell, T. A., Lee, A., de Andrade, E. S., et al. 2023, matplotlib/matplotlib:REL: v3.7.1, Zenodo, doi:10.5281/zenodo.7697899
 Chan, C., & Müller, B. 2020, *MNRAS*, **496**, 2000
 Cheong, P. C.-K., Lam, A. T.-L., Ng, H. H.-Y., & Li, T. G. F. 2021, *MNRAS*, **508**, 2279
 Cheong, P. C.-K., Lin, L.-M., & Li, T. G. F. 2020, *CQGra*, **37**, 145015
 Cheong, P. C.-K., Pong, D. Y. T., Yip, A. K. L., & Li, T. G. F. 2022, *ApJS*, **261**, 22
 Commerçon, B., Teyssier, R., Audit, E., Hennebelle, P., & Chabrier, G. 2011, *A&A*, **529**, A35
 Davis, S. W., Stone, J. M., & Jiang, Y.-F. 2012, *ApJS*, **199**, 9
 Deppe, N., Thrope, W., Kidder, L. E., et al. 2022, SpECTRE v2022.04.04, Zenodo, doi:10.5281/zenodo.6412468
 Dessart, L., Ott, C. D., Burrows, A., Rosswog, S., & Livne, E. 2009, *ApJ*, **690**, 1681
 Dubroca, B., & Feugeas, J. 1999, *CRASM*, **329**, 915
 Estee, J., Lynch, W. G., Tsang, C. Y., et al. 2021, *PhRvL*, **126**, 162701
 Fernández, R., Tchekhovskoy, A., Quataert, E., Foucart, F., & Kasen, D. 2019, *MNRAS*, **482**, 3373
 Foglizzo, T., Kazeroni, R., Guilet, J., et al. 2015, *PASA*, **32**, e009
 Foucart, F. 2018, *MNRAS*, **475**, 4186
 Foucart, F. 2023, *LRCA*, **9**, 1
 Foucart, F., Duez, M. D., Hébert, F., et al. 2021, *ApJ*, **920**, 82
 Foucart, F., Haas, R., Duez, M. D., et al. 2016a, *PhRvD*, **93**, 044019
 Foucart, F., O'Connor, E., Roberts, L., et al. 2015, *PhRvD*, **91**, 124021
 Foucart, F., O'Connor, E., Roberts, L., et al. 2016b, *PhRvD*, **94**, 123016
 Fragile, P. C., Etheridge, S. M., Anninos, P., Mishra, B., & Kluźniak, W. 2018, *ApJ*, **857**, 1
 Fragile, P. C., Gillespie, A., Monahan, T., Rodriguez, M., & Anninos, P. 2012, *ApJS*, **201**, 9
 Fragile, P. C., Olejar, A., & Anninos, P. 2014, *ApJ*, **796**, 22
 Fujibayashi, S., Kiuchi, K., Nishimura, N., Sekiguchi, Y., & Shibata, M. 2018, *ApJ*, **860**, 64
 Fujibayashi, S., Sekiguchi, Y., Kiuchi, K., & Shibata, M. 2017, *ApJ*, **846**, 114
 Fujibayashi, S., Shibata, M., Wanajo, S., et al. 2020a, *PhRvD*, **101**, 083029
 Fujibayashi, S., Wanajo, S., Kiuchi, K., et al. 2020b, *ApJ*, **901**, 122
 Galeazzi, F., Kastaun, W., Rezzolla, L., & Font, J. A. 2013, *PhRvD*, **88**, 064009

- González, M., Audit, E., & Huynh, P. 2007, *A&A*, **464**, 429
- Harris, C. R., Millman, K. J., van der Walt, S. J., et al. 2020, *Natur*, **585**, 357
- Harten, A., Lax, P., & Leer, B. 1983, *SIAMR*, **25**, 35
- Hunter, J. D. 2007, *CSE*, **9**, 90
- Izquierdo, M. R., Pareschi, L., Miñano, B., Massó, J., & Palenzuela, C. 2023, *CQGra*, **40**, 145014
- Janka, H.-T. 2012, *ARNPS*, **62**, 407
- Just, O., Goriely, S., Janka, H. T., Nagataki, S., & Bauswein, A. 2022, *MNRAS*, **509**, 1377
- Just, O., Obergaulinger, M., & Janka, H. T. 2015, *MNRAS*, **453**, 3386
- Kaneko, N., Morita, K., & Maekawa, M. 1984, *Ap&SS*, **107**, 333
- Kawaguchi, K., Fujibayashi, S., & Shibata, M. 2023, *PhRvD*, **107**, 023026
- Kuroda, T., Takiwaki, T., & Kotake, K. 2016, *ApJS*, **222**, 20
- Laiu, M. P., Endeve, E., Chu, R., Harris, J. A., & Messer, O. E. B. 2021, *ApJS*, **253**, 52
- Lattimer, J. M., & Swesty, D. F. 1991, *NuPhA*, **535**, 331
- Lentz, E. J., Bruenn, S. W., Hix, W. R., et al. 2015, *ApJL*, **807**, L31
- Levermore, C. D. 1984, *JQSRT*, **31**, 149
- Levermore, C. D., & Pomraning, G. C. 1981, *ApJ*, **248**, 321
- Liebrandt, M., Rapp, M., Janka, H. T., & Mezzacappa, A. 2005, *ApJ*, **620**, 840
- Löhner, R. 1987, *CMAME*, **61**, 323
- López-Miralles, J., Martí, J. M., & Perucho, M. 2023, *CoPhC*, **284**, 108630
- Lowrie, R. B., Mihalas, D., & Morel, J. E. 2001, *JQSRT*, **69**, 291
- Marek, A., Dimmelmeier, H., Janka, H. T., Müller, E., & Buras, R. 2006, *A&A*, **445**, 273
- McClarren, R. G., & Hauck, C. D. 2010, *JCoPh*, **229**, 5597
- McKinney, J. C., Tchekhovskoy, A., Sadowski, A., & Narayan, R. 2014, *MNRAS*, **441**, 3177
- McKinney, W. 2010, in Proc. of the 9th Python in Science Conf., ed. S. van der Walt & J. Millman, 56
- Melon Fuksman, J. D., & Mignone, A. 2019, *ApJS*, **242**, 20
- Melson, T., Janka, H.-T., Bollig, R., et al. 2015, *ApJL*, **808**, L42
- Metzger, B. D., & Fernández, R. 2014, *MNRAS*, **441**, 3444
- Mewes, V., Zlochower, Y., Campanelli, M., et al. 2020, *PhRvD*, **101**, 104007
- Mezzacappa, A., Endeve, E., Messer, O. E. B., & Bruenn, S. W. 2020, *LRCA*, **6**, 4
- Miller, J. M., Ryan, B. R., Dolence, J. C., et al. 2019, *PhRvD*, **100**, 023008
- Minerbo, G. N. 1978, *JQSRT*, **20**, 541
- Montero, P. J., Baumgarte, T. W., & Müller, E. 2014, *PhRvD*, **89**, 084043
- Müller, B., Janka, H.-T., & Dimmelmeier, H. 2010, *ApJS*, **189**, 104
- Munier, A., & Weaver, R. 1986, *CoPhR*, **3**, 127
- Murchikova, E. M., Abdikamalov, E., & Urbatsch, T. 2017, *MNRAS*, **469**, 1725
- Nagakura, H., Iwakami, W., Furusawa, S., et al. 2017, *ApJS*, **229**, 42
- Nagakura, H., Sumiyoshi, K., & Yamada, S. 2014, *ApJS*, **214**, 16
- Nedora, V., Bernuzzi, S., Radice, D., et al. 2019, *ApJL*, **886**, L30
- Neilsen, D., Liebling, S. L., Anderson, M., et al. 2014, *PhRvD*, **89**, 104029
- O'Connor, E., Bollig, R., Burrows, A., et al. 2018, *JPhG*, **45**, 104001
- O'Connor, E., & Ott, C. D. 2010, *CQGra*, **27**, 114103
- O'Connor, E., & Ott, C. D. 2013, *ApJ*, **762**, 126
- O'Connor, E. P., & Couch, S. M. 2018a, *ApJ*, **865**, 81
- O'Connor, E. P., & Couch, S. M. 2018b, *ApJ*, **854**, 63
- O'Connor, E. 2015, *ApJS*, **219**, 24
- pandas development team 2020, pandas-dev/pandas: Pandas v2.0.3, Zenodo, doi:10.5281/zenodo.3509134
- Pareschi, L., & Russo, G. 2005, *JCom*, **25**, 129
- Perego, A., Radice, D., & Bernuzzi, S. 2017, *ApJL*, **850**, L37
- Perego, A., Rosswog, S., Cabezón, R. M., et al. 2014, *MNRAS*, **443**, 3134
- Pili, A. G., Bucciantini, N., & Del Zanna, L. 2014, *MNRAS*, **439**, 3541
- Pili, A. G., Bucciantini, N., & Del Zanna, L. 2015, *MNRAS*, **447**, 2821
- Pili, A. G., Bucciantini, N., & Del Zanna, L. 2017, *MNRAS*, **470**, 2469
- Pomraning, G. C. 1981, *JQSRT*, **26**, 385
- Pons, J. A., Ibáñez, J. M., & Miralles, J. A. 2000, *MNRAS*, **317**, 550
- Press, W. H., Teukolsky, S. A., Vetterling, W. T., & Flannery, B. P. 1996, Numerical Recipes in Fortran 90, Vol. 2 (Cambridge: Cambridge Univ. Press)
- Radice, D., Abdikamalov, E., Rezzolla, L., & Ott, C. D. 2013, *JCoPh*, **242**, 648
- Radice, D., Bernuzzi, S., Perego, A., & Haas, R. 2022, *MNRAS*, **512**, 1499
- Radice, D., Rezzolla, L., & Galeazzi, F. 2015, in ASP Conf. Ser. 498, Numerical Modeling of Space Plasma Flows ASTRONUM-2014, ed. N. V. Pogorelov, E. Audit, & G. P. Zank (San Francisco, CA: ASP), 121
- Rampp, M., & Janka, H. T. 2002, *A&A*, **396**, 361
- Richers, S. 2020, *PhRvD*, **102**, 083017
- Rivera-Paleo, F. J., & Guzmán, F. S. 2019, *ApJS*, **241**, 28
- Roberts, L. F., Ott, C. D., Haas, R., et al. 2016, *ApJ*, **831**, 98
- Roe, P. L. 1986, *AnRFM*, **18**, 337
- Ryan, B. R., & Dolence, J. C. 2020, *ApJ*, **891**, 118
- Santos-Pérez, S., Obergaulinger, M., & Cordero-Carrión, I. 2023, arXiv:2302.12089
- Sekiguchi, Y., Kiuchi, K., Kyutoku, K., & Shibata, M. 2015, *PhRvD*, **91**, 064059
- Sekiguchi, Y., Kiuchi, K., Kyutoku, K., Shibata, M., & Taniguchi, K. 2016, *PhRvD*, **93**, 124046
- Shen, G., Horowitz, C. J., & Teige, S. 2011, *PhRvC*, **83**, 035802
- Shibata, M., Kiuchi, K., Sekiguchi, Y., & Suwa, Y. 2011, *PThPh*, **125**, 1255
- Sądowski, A., Narayan, R., Tchekhovskoy, A., & Zhu, Y. 2013, *MNRAS*, **429**, 3533
- Skinner, M. A., Dolence, J. C., Burrows, A., Radice, D., & Vartanyan, D. 2019, *ApJS*, **241**, 7
- Skinner, M. A., & Ostriker, E. C. 2013, *ApJS*, **206**, 21
- Smit, J. M., Cernohorsky, J., & Dullemond, C. P. 1997, *A&A*, **325**, 203
- Sumiyoshi, K., & Yamada, S. 2012, *ApJS*, **199**, 17
- Takahashi, H. R., & Ohsuga, K. 2013, *ApJ*, **772**, 127
- Takahashi, H. R., Ohsuga, K., Kawashima, T., & Sekiguchi, Y. 2016, *ApJ*, **826**, 23
- Thorne, K. S. 1981, *MNRAS*, **194**, 439
- Turk, M. J., Smith, B. D., Oishi, J. S., et al. 2011, *ApJS*, **192**, 9
- van Leer, B. 1974, *JCoPh*, **14**, 361
- Virtanen, P., Gommers, R., Oliphant, T. E., et al. 2020, *NatMe*, **17**, 261
- Wanajo, S., Sekiguchi, Y., Nishimura, N., et al. 2014, *ApJL*, **789**, L39
- Weih, L. R., Gabbana, A., Simeoni, D., et al. 2020, *MNRAS*, **498**, 3374
- Weih, L. R., Olivares, H., & Rezzolla, L. 2020, *MNRAS*, **495**, 2285
- White, C. J., Mullen, P. D., Jiang, Y.-F., et al. 2023, *ApJ*, **949**, 103
- Woolsey, S. E., & Weaver, T. A. 1995, *ApJS*, **101**, 181
- Zanotti, O., Roedig, C., Rezzolla, L., & Del Zanna, L. 2011, *MNRAS*, **417**, 2899